

Robust interferometric imaging via prior-less phase recovery: redundant spacing calibration with generalized closure phases

Binoy G. Kurien,^{1,2}★ Jonathan B. Ashcom,² Vinay N. Shah,² Yaron Rachlin,² Vahid Tarokh¹

¹*Harvard Paulson School of Engineering and Applied Sciences, 29 Oxford St., Cambridge, MA, 02138*

²*MIT Lincoln Laboratory, 244 Wood St., Lexington, MA 02421*

Accepted XXX. Received YYY; in original form ZZZ

ABSTRACT

Redundant Spacing Calibration (RSC) techniques employ redundancy in the baselines of a telescope array to eliminate the contribution of atmospheric turbulence in the interferometric observables. Whereas conventional techniques for this elimination require the enforcement of prior constraints on the underlying image, RSC algorithms can be, in principle, mathematically well-posed and hence require no such prior knowledge. Traditionally these algorithms have been applied directly to the fringe measurements. However, in scenarios of low photon flux, such as those arising in the observation of dim objects in space, single-exposure fringe measurements are not reliable observables in general. Instead one must rely on time-averaged, atmosphere-invariant quantities such as the bispectrum. In this paper, we develop a novel algorithm for redundant arrays which provides robust image reconstruction using integrable atmosphere-invariant observables. Our algorithm utilizes standard linear estimation methods, as well as techniques from lattice theory, to reliably estimate the Fourier phase. Moreover, we provide theoretical and empirical evidence that generalizing the classical bispectrum to higher-order atmosphere-invariant observables, which we call *n-spectra*, can offer significant performance gains. Our selection of an independent and high-SNR set of n-spectra leverages the notion of the *minimum cycle basis* from graph theory. We analyze the expected shot-noise-limited performance of our algorithm for both pairwise and Fizeau interferometric architectures, and corroborate this analysis with simulation results showing performance near the Cramer-Rao bound. Lastly, we apply techniques from the field of *compressed sensing* to perform image reconstruction from the estimated complex visibilities.

Key words: techniques: interferometric – techniques: image processing – atmospheric effects – methods: analytical – methods: numerical

1 INTRODUCTION

Interferometers can produce high-resolution imagery of a distant object by combining signals collected by an array of apertures. Assuming the spatial extent of the array is sufficiently large, they can in principle achieve the resolution of a single aperture of prohibitively large size. The critical measurement enabling image reconstruction is the time-averaged, pairwise cross-correlation between the fields observed at each aperture in the array.

This measurement is typically obtained via computation in radio interferometers, since at radio wavelengths the fields can be sampled and correlated digitally. Optical interferometers, on the other hand, obtain the correlation indirectly, by measuring the intensity of the *interference fringe*, i.e. superposition of the fields incident at each aperture. As established by the van-Cittert Zernike Theorem (van Cittert 1934) (Zernike 1938), each correlation provides a sample of the scene's 2D Fourier Transform. Over the past few decades, a diverse set of algorithms has been developed to reconstruct an image of the scene from these samples.

★ Email: bkurien@ll.mit.edu

A principal challenge in interferometric image reconstruction is variation in the complex gains among the multiple apertures of the interferometer. This variation can arise from differences among the analog components of the antenna elements (e.g. cable length differences) in the array. Moreover, atmospheric turbulence alters the effective path length (or *optical piston*) from the target to each telescope by a non-uniform and time-varying amount. For simplicity, we will henceforth refer to such aperture-specific phase variation as *optical path difference* (OPD), regardless of its source. As a result of OPD, the Fourier component measured by apertures k and j is given by $y_{kj} = |y_{kj}|e^{i\beta_{kj}}$, in which $\beta_{kj} = (\theta_{kj} + \delta\phi_{kj}) \bmod 2\pi$, and θ_{kj} is the true Fourier phase at spatial frequency $\frac{\mathbf{b}_{kj}}{\lambda}$, and $\delta\phi_{kj}$ represents the OPD observed between apertures k and j . In a non-redundant array of N apertures, there are $\binom{N}{2}$ such measurements corresponding to each pair of apertures. Collecting such measurements together, we obtain a system of equations:

$$\mathbf{\beta} = \mathbf{\theta} + \mathbf{A}\phi \quad (1)$$

where \mathbf{A} is an $\binom{N}{2} \times N$ matrix whose rows contain the piston differences involved in each measurement.

Since there are $\binom{N}{2}$ unknown Fourier phases and $N - 1$ unknown OPDs, inference of the Fourier phases from the $\binom{N}{2}$ phase measurements is inherently ill-posed for such a non-redundant array. The traditional means of mitigating this issue has been to impose additional prior constraints on the image to compensate for this degeneracy. For example, many popular methods assume and enforce smoothness of the image by bounding its *total variation*¹ (Rudin et al. 1992). Other effective approaches favor a pixel distribution of high entropy (Skilling & Bryan 1984).

Reconstruction in optical interferometry amounts to finding an image within prior constraints that also agrees with the observed data. To achieve this objective, a myriad of so-called *self-calibration* algorithms were developed in radio astronomy (see, e.g., Pearson & Readhead (1984) and Besnerraïs et al. (2008)) which alternate between estimation of the Fourier phases and estimation of the image coefficients subject to the imposed constraints. Such algorithms have shown to be successful in high-flux scenarios in which the interferometric measurements have a high signal-to-noise ratio (SNR). In low-flux scenarios on the other hand, one must integrate observables over a long time period in order to build sufficient SNR for reliable image reconstruction. Since integration beyond the coherence time of the atmosphere would result in fringe blurring, one is then led to the formation and subsequent integration of atmosphere-invariant observables from each atmosphere-coherence time (or *frame*). The classic of these observables is the triple product of the Fourier components along the sides of a baseline triangle (e.g. \mathbf{b}_{12} , \mathbf{b}_{23} , and \mathbf{b}_{31}). Note that the OPD cancels in these products and hence, like the Fourier magnitudes, these so-called *bispectra*² are OPD-invariant observables. However,

for a non-redundant array with $\binom{N}{2}$ distinct baselines, recovery of the Fourier phases from the bispectra phases (i.e. the *closure phases*) remains ill-posed since there are only $\binom{N-1}{2}$ independent bispectra (Readhead et al. 1988). Successful bispectra-based image reconstruction remains feasible in spite of this ill-posedness (see e.g. Thiébaut (2013), Besnerraïs et al. (2008)), but again prior constraints (e.g. on the image support) must be enforced to regularize the reconstruction. It is well-known that such prior-regularized approaches become unreliable when the scene under observation does not match the prior assumptions being enforced.

As interferometric systems are tasked with the observation of increasingly-complex scenes, approaches which minimize reliance on specialized prior assumptions are expected to gain appeal. An alternative and intrinsically well-posed approach to prior-regularized phase recovery is to use baseline redundancy to explicitly solve for OPD variation; an array with baseline redundancy contains repeated instances of the same baseline involving distinct aperture pairs. Since Fourier phases can be assumed to be equal for all repeated baselines, an observed difference amongst their corresponding measurements exposes the contribution of the OPD. This idea of using redundant arrays to calibrate out OPD variation, known as *Redundant Spacing Calibration* (RSC), was developed in works such as those by Hamaker et al. (1977), Arnot et al. (1985) and Greenaway (1990). In recent years, innovation in optical technology has engendered a revival of interest in the RSC technique. The simultaneous (or *Fizeau*-style) measurement of fringes on a common focal plane has long been a popular method of acquiring many baseline measurements in an economical manner. However, the Fizeau method had been incompatible with RSC techniques since the fringes formed by each set of redundant baselines would alias on the focal plane. An elegant solution to this problem was proposed by Perrin et al. (2006). This work developed the idea of segmenting the entrance pupil of a single telescope into an RSC arrangement of sub-pupils from which the light was then coupled via single-mode fiber to a non-redundant exit pupil, thereby permitting unambiguous and simultaneous fringe detection for an RSC array. Current systems leveraging this so-called *pupil-remapping* architecture include the FIRST (see e.g. Perrin et al. (2006) and Huby, E. et al. (2013)) and DRAGON-FLY (Jovanovic et al. 2012) instruments, both of which were designed with the mission of imaging faint objects in space such as exoplanets. A phase recovery algorithm for the case of a redundant front-end was proposed by Lacour et al. (2007). The algorithmic framework developed in this paper is directly applicable to this architecture.

While the classical RSC algorithms cited above have been applied successfully in both the optical and radio realms, their applicability is limited in the former relative to the latter. Observation at radio wavelengths is typically limited by background noise rather than by shot noise, which typically limits performance at optical wavelengths. As a result,

¹ The total variation of an image is defined as the integral of the absolute value of the image gradient.

² It is customary in the literature to use *bispectrum* to refer to the entire function multiplying Fourier samples

along a given triangle of spatial frequencies. We will use the term *bispectra* to refer to particular samples of this function.

the relative strength of the image Fourier components (i.e. the *visibility function*) declines more gradually with increasing baseline length in the former relative to the latter (Buscher 2015). This in turn generally makes fringe tracking a viable option for stabilizing the phase measured by each baseline in a radio telescope array, and in such cases RSC-based inference techniques can operate directly on the stabilized Fourier phasors. We will refer to such techniques as *direct* techniques. Direct techniques have been implemented as the calibration scheme of choice for several radio interferometers: the Donald C. Backer Precision Array for Probing the Epoch of Reionization (PAPER) in South Africa (see Ali et al. (2015)), the MIT Epoch of Reionization (MITeOR) in the United States (see Zheng et al. (2014)), and the Ooty Radio Telescope (ORT) in India (see Marthi & Chengalur (2014)). The rapid decay in SNR with baseline length commonly observed at optical wavelengths, on the other hand, entails integration of *atmosphere-invariant* observables (e.g. the bispectra) over multiple atmospheric coherence times in the case of dim-target observation. While the observables may differ, there are important parallels to be noted. Firstly, the ability of RSC techniques to recover the Fourier phase with no prior knowledge about the target is retained with atmosphere-invariant observables as we will see. Secondly, in direct and atmosphere-invariant approaches, there are two principal algorithmic approaches for phase recovery: those that operate on the phasor of the observed complex visibilities (respectively, the bispectra), and those that operate on their phase (respectively, the closure phase). An important issue encountered in both approaches is the issue of integer phase ambiguities, which manifests itself as phase wrapping in phase-based approaches, and false minima in the phasor-based approaches. Array design considerations based on the notion of *wrap-invariance* (Kurien et al. 2016), as well as algorithms from lattice theory (Lannes & Anterrieu 1999), have been used to understand and solve these ambiguity issues in the case of direct observation. Our case for the reliability of our methods will include an extension of these principles to inference from atmosphere-invariants.

In this paper, we develop a novel algorithmic framework for imaging dim, complex objects using atmosphere-invariant observables formed by a redundant configuration of a large number of optical telescopes or sub-apertures. As such, this framework may prove useful to astronomers processing data from existing systems like those mentioned above, as well as to the designers of new large-scale instruments such as the future Planet Formation Imager (PFI) (Kraus et al. 2014), which seeks to develop an understanding of the processes governing the very assembly of planetary systems from interstellar dust. To the best our knowledge, work by Lannes & Anterrieu (1999) was the first to explore the use of such atmosphere-invariant observables in the explicit context of RSC-based phase recovery. In this work, the authors develop a pseudo-inverse estima-

tor which recovers the Fourier phases from the measured baseline phases via an intermediate computation of the closure phases. The computation of the necessary covariance matrices for optimal estimation within this formulation is omitted. Since it is in fact the closure phases which are the direct observables in practical low-flux scenarios, we present instead an approach working solely with the closure phases and compute the necessary covariances in straightforward manner. Lannes (2003) later proposed an alternate estimator based on computation of the Smith Normal Form of the matrix mapping Fourier phases to closure phases. This estimator has the advantage of completely eliminating the effect of phase wrapping in the closure measurements when appropriate routines from lattice theory are used to pre-process the phase measurements. In contrast, our estimator reliably uses standard, fast linear estimation techniques, thereby obviating computation of the Smith Normal Form at the possible expense of an extra shift in the recovered image. Such image shifts are anticipated to be of negligible importance in most cases of practical interest.

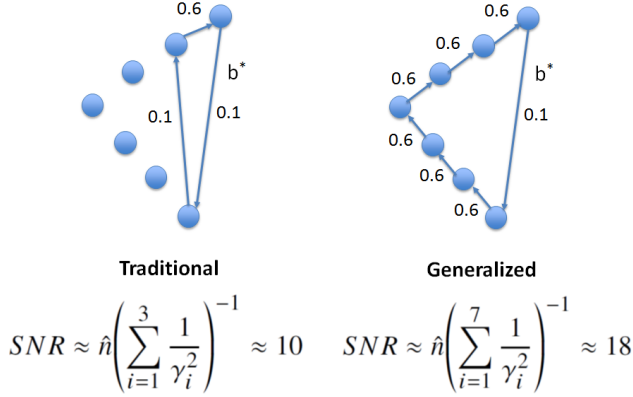
An important novel aspect of our framework is its generalization of the bispectrum observable for the purposes of increased sensitivity. Though the bispectrum and its associated closure phase have been standard interferometric observables for decades after the latter was first proposed by Jennison (1958), it is not difficult to imagine situations in which use of these observables unnecessarily limits reconstruction performance. In Figure 1, we illustrate this idea with an example. We label each baseline of an interferometric array with a visibility, which is an indicator of the strength of its Fourier component relative to the overall brightness of the image. In accordance with the power-law decay of intensity with spatial-frequency modulus in an overwhelmingly-large fraction of natural images (see, e.g. Ruderman (1994)), we consider a visibility distribution which drops sharply with baseline length. In standard **bispectral** imaging, the high-spatial-frequency phase information associated with long baseline b^* is recovered via forming a **closure triangle**, for example, with a short baseline along with another long baseline (*Traditional*). As we will see, for a certain range of photon fluxes, the SNR of the bispectrum is roughly proportional to the sum of the reciprocals of the squared visibilities of the associated baselines (Kulkarni et al. 1991), i.e.:

$$SNR \approx \hat{n} \left(\sum_{i=1}^3 \frac{1}{\gamma_i^2} \right)^{-1} \quad (2)$$

where \hat{n} is the number of photoelectrons (pe) received per interference fringe per exposure frame. As we will show in this paper, this SNR model extends in the natural way to the SNR of higher-order observables like that shown on the right (*Generalized*). In contrast with the *Traditional* observable, *Generalized* observable utilizes only short (high-visibility) baselines to close the long baseline, resulting in a near-doubling of the resulting SNR. We will henceforth refer to the higher-order generalization of the bispectrum triple product as the *n-spectrum*, and its phase as the *generalized closure phase*. The statistics for these new observables will be derived in the course of this paper.

Generalization of the closure phase is not a novel con-

Figure 1. Generalizing the phase closure concept. SNRs given assume each aperture contributes $\hat{n} = 2e3$ photoelectrons to each fringe in pairwise combination.



cept in the astronomical community. [Lannes \(1991\)](#) defined the general class of matrices which annihilate the subspace comprising all possible OPD vectors. Recently [Martinache \(2010\)](#) proposed one convenient construction of such matrices as the orthogonal basis for the left-nullspace of the matrix \mathbf{A} in Equation (1). The vectors of this basis are assembled as the rows of a matrix \mathbf{K} . When this matrix is applied to the measurements β , the atmosphere-induced ϕ contributions clearly cancel, leaving only linear combinations of the object phases in θ . These linear combinations, known as *kernel phases*, can then be used to reconstruct the Fourier phase via direct application of the pseudo-inverse of \mathbf{K} ([Martinache 2014](#)), or via regularized inversion using prior image models ([Ireland 2013](#)). While kernel phases can serve well as observables for single-exposure mapping, they, like their closure phase counterparts, may fail to average reliably. Indeed, except for the case in which the kernel phase is confined to a narrow region in the phase domain away from $\pm\pi$ (e.g. in a scenario in which the per-frame flux is high and/or the target is highly compact), the inherent 2π -wrapping of the phase renders the the averaged kernel phase a poor estimator of the true kernel phase in general ³. In this paper we consider the scenario of observing a complex target with a long-baseline interferometer, in which the histogram of measured baseline phases (and hence their linear combinations) will approach a uniform distribution at a suitably-low visibility. In such cases, it is necessary to integrate the corresponding atmosphere-invariant phasor quantities, i.e. the *n-spectra* defined above, and then extract their phase as a reliable observable.

Assuming the Fourier phases can be estimated accurately from the atmosphere-invariant observables, image reconstruction essentially reduces to the same frequency-undersampled problem encountered in a plethora of other fields including medical imaging as well as radio astronomy. The fundamental problem in the latter is to regularize the

³ The reader is directed to [Buscher \(2015\)](#) for a more detailed discussion of this issue.

ill-posed reconstruction of N_{resEl} resolution elements from $m \ll N_{resEl}$ spatial frequency measurements corresponding to the available baseline pairs in the telescope array. Traditionally approaches based on the so-called *CLEAN* algorithm due to [Högbom \(1974\)](#), which implicitly fit the measurements to an image model consisting of a sparse collection of point-like sources, have been used to solve this problem. Given the success of this relatively-simple algorithm, it is hardly surprising that recently-developed techniques leveraging sophisticated sparse image models (see e.g. [Wiaux et al. \(2009\)](#), [Baron et al. \(2010\)](#), [Kurien et al. \(2014\)](#)) have shown promise. In fact such algorithms belong to a burgeoning family of cross-disciplinary techniques, which are based on seminal work within the last decade ([Donoho 2006](#)), ([Candès et al. 2006](#)), in the field of *compressed sensing*.

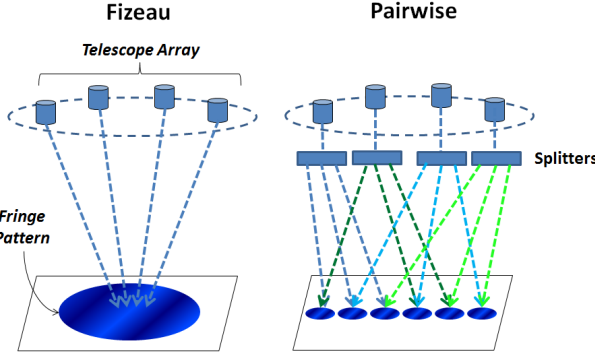
In this paper, we develop a comprehensive algorithmic framework for image reconstruction based on RSC techniques and compressed sensing, and analyze its performance for the two popular beam-combining architectures used in optical interferometry (*pairwise*, and *Fizeau*). The paper is organized as follows. In Section II, we derive an SNR model for the *n-spectrum*, as well as for the covariance amongst distinct *n-spectra*. The analysis begins with the pairwise case for simplicity, and mathematical arguments for an extension to the Fizeau case are presented at the end of the section and in the Appendix. In Section III, we describe a systematic, integer-least-squares approach for reconstructing imagery from object visibilities and generalized closure phases (GC). We draw on the notion of a *minimum cycle basis* to select a minimum set of linearly-independent GC's (i.e. a *basis*) of minimum variance which spans the subspace of all closures. Leveraging techniques first suggested by [Lannes & Anterrieu \(1999\)](#) and the notion of *wrap-invariant* measurement mappings introduced in [Kurien et al. \(2016\)](#), we apply algorithms from lattice theory to unwrap the generalized closures. We then quantify the gain in theoretical performance afforded by generalizing the classical third-order atmosphere-invariant observables to higher-order cycles, and corroborate this theoretical performance with simulation results. In this simulation, we apply our algorithm to reconstruct a dim, structured object from generalized closures. For the final image reconstruction, we employ a sparse recovery algorithm which enforces smoothness in the image domain by minimizing the aforementioned *total variation* metric.

2 PRELIMINARIES

2.1 Interferometric Architectures

In this paper we consider two popular beam combination architectures in use in optical interferometry: the pairwise combination scheme, and the Fizeau combination scheme. The two schemes are illustrated in Figure 2 below. Suppose we have a telescope array consisting of N_{ap} apertures. In the pairwise scheme, light from each aperture is split N_{ap} ways and combined with each other aperture. Hence each of the $\binom{N_{ap}}{2}$ focal planes receives a small fraction of the total signal $\frac{2n}{N_{ap}-1}$ photons, and thus incurs the shot noise from only two apertures. In the Fizeau scheme, a single focal

Figure 2. The two popular beam combination schemes in optical interferometry



plane receives all of the light collected by the array (i.e. $N_{ap}n$ photons), and incurs the shot noise from all N_{ap} apertures.

In this paper we analyze the performance of generalized-closure-based imaging for both architectures in terms of mean-squared error (MSE) of the phase estimates. We begin with the pairwise architecture since it is significantly easier to analyze. We then present a series of approximations which accurately describe the algorithm's performance in the Fizeau case while keeping the tediousness of the mathematics at a manageable level. In both cases, the analysis is based on the computation of the moments of the Poisson distribution; in the pairwise case, the first two moments are required, whereas in the Fizeau case, **the first t moments are needed, where t is the order of the generalized closure.**

2.2 Fringe Noise Model for Pairwise Beam Combiner

Given N_{ap} apertures, recall that the Fourier phase and amplitude of the object is encoded in a series of $\binom{N_{ap}}{2}$ interference fringes observed on a focal plane. In the pairwise case, each fringe is measured on a separate set of detectors so that the Poisson shot noise incurred is independent for each fringe. Suppose each aperture receives n photons and that this light is split evenly (e.g. by a beam-splitter) before being combined with the light from the other apertures. Hence each aperture contributes $\hat{n} = \frac{n}{N_{ap}-1}$ photons to each fringe. The expectation of number of photons q at a given detector k for a given fringe is given by:

$$\langle q(k) \rangle = \frac{2\hat{n}}{N_p} (1 + \gamma \cos(\omega k + \theta + \phi)) \quad (3)$$

where N_p is the number of pixels over which these photons are spread, γ is the visibility of the fringe (which takes its value between 0 and 1), ω is the fringe frequency, θ is the Fourier phase, and ϕ is the atmosphere phase.

To retrieve the object phase and amplitude from its fringe encoding, we simply take the Fourier transform and evaluate it at the fringe frequency:

$$z = \sum_{k=0}^{N_p-1} q(k) e^{-i\omega k} \quad (4)$$

To obtain the bispectrum SNR, it will be useful to compute the power in the fringe, i.e. expectation of the quantity zz^* :

$$\langle zz^* \rangle = \left\langle \sum_{k=0}^{N_p-1} \sum_{k'=0}^{N_p-1} q(k) q(k') e^{-i\omega k} e^{i\omega k'} \right\rangle \quad (5)$$

This is equivalent to:

$$\langle zz^* \rangle = \sum_{k=0}^{N_p-1} \sum_{k'=0}^{N_p-1} \langle q(k) q(k') \rangle e^{-i\omega k} e^{i\omega k'} \quad (6)$$

Using the first two moments of the Poisson distribution, we can write:

$$\langle q(k) q(k') \rangle = \langle q(k) \rangle \langle q(k') \rangle + \delta_{kk'} \langle q(k) \rangle \quad (7)$$

Substituting into Equation (6), we obtain:

$$\langle zz^* \rangle = \sum_{k=0}^{N_p-1} \langle q(k) \rangle e^{-i\omega k} \sum_{k'=0}^{N_p-1} \langle q(k') \rangle e^{i\omega k'} + \sum_{k=0}^{N_p-1} \langle q(k) \rangle \quad (8)$$

Simplifying we obtain:

$$\langle zz^* \rangle = \gamma^2 \hat{n}^2 + 2\hat{n} \quad (9)$$

2.3 N-Spectrum Covariance and SNR Models for the Pairwise Architecture

Let us define a *generalized N-spectrum* G as the product of complex fringe phasors along an t -edge cycle. Given variances $\sigma_{Re}^2(G)$ and $\sigma_{Im}^2(G)$ of real and imaginary components, respectively, we define the pseudo-variance of the product as:

$$V_{pairwise}(G) := \sigma_{Re}^2 + \sigma_{Im}^2 = \langle GG^* \rangle - \langle G \rangle \langle G^* \rangle \quad (10)$$

or:

$$V_{pairwise}(G) = \left[\prod_{i=1}^t \langle z_i z_i^* \rangle \right] - \prod_{i=1}^t \langle z_i \rangle \langle z_i^* \rangle \quad (11)$$

$$V_{pairwise}(G) = \left[\prod_{i=1}^t (\hat{n}^2 \gamma_i^2 + 2\hat{n}) \right] - \hat{n}^{2t} \prod_{i=1}^t \gamma_i^2 \quad (12)$$

In the specific case of the classic triple product (i.e. the *bispectrum*), this expands to (Kulkarni et al. 1991):

$$V_{pairwise}(G) = 2\hat{n}^5 (\gamma_1^2 \gamma_2^2 + \gamma_2^2 \gamma_3^2 + \gamma_3^2 \gamma_1^2) + 4\hat{n}^4 (\gamma_1^2 + \gamma_2^2 + \gamma_3^2) + 8\hat{n}^3 \quad (13)$$

The SNR $S_{pairwise} := \frac{\sqrt{2}|G|}{\sqrt{V(G)}}$ is then given by:

$$S_{pairwise} = \frac{\gamma_1 \gamma_2 \gamma_3 \hat{n}^{\frac{3}{2}}}{\sqrt{\hat{n}^2 (\gamma_1^2 \gamma_2^2 + \gamma_2^2 \gamma_3^2 + \gamma_3^2 \gamma_1^2) + 2\hat{n} (\gamma_1^2 + \gamma_2^2 + \gamma_3^2) + 4}} \quad (14)$$

To gain insight into the limiting behavior of the SNR, we make two approximations: A low-SNR approximation can

be found by considering only the constant term in the denominator, which will dominate when \hat{n} and/or the γ_i are small.

$$S_{\text{pairwise,low}} \approx \frac{\gamma_1 \gamma_2 \gamma_3 \hat{n}^{\frac{3}{2}}}{2} \quad (15)$$

A high-SNR approximation can be found by considering the highest-order term in the denominator, which will dominate when \hat{n} is large and/or the γ_i are large.

$$S_{\text{pairwise,high}} \approx \frac{\gamma_1 \gamma_2 \gamma_3 \hat{n}^{\frac{3}{2}}}{\sqrt{\hat{n}^2(\gamma_1^2 \gamma_2^2 + \gamma_2^2 \gamma_3^2 + \gamma_3^2 \gamma_1^2)}} \quad (16)$$

By averaging the fringe phasors over a sufficient number of frames N_f , we can build the SNR to a level at which the bispectrum phase (i.e. the *closure*) phase can be measured. For phasor SNRs sufficiently greater than 1, the following approximation holds for the variance on the closure phase θ_{cl} :

$$\sigma_{\theta_{cl}}^2 \approx \frac{1}{N_f S^2} \quad (17)$$

We then obtain the following approximations for the closure phase variances. At low SNR, we have:

$$\sigma_{\theta_{cl,low}}^2 \approx \frac{4}{N_f \gamma_1^2 \gamma_2^2 \gamma_3^2 \hat{n}^3} \quad (18)$$

Taking the logarithm we find that the variance decouples:

$$\log \sigma_{\theta_{cl,low}}^2 \approx -2 \log \gamma_1 - 2 \log \gamma_2 - 2 \log \gamma_3 - 3 \log \hat{n} + C \quad (19)$$

where C is a constant independent of the flux level \hat{n} and the visibilities γ_i .

At high SNR, we have:

$$\sigma_{\theta_{cl,high}}^2 \approx \frac{1}{\hat{n} N_f} \left(\frac{1}{\gamma_1^2} + \frac{1}{\gamma_2^2} + \frac{1}{\gamma_3^2} \right) \quad (20)$$

Generalizing the results above to n-spectra, we obtain for low SNR,

$$\sigma_{\theta_{cl,low}}^2 \approx \frac{2^t}{N_f \hat{n}^t \prod_{i=1}^t \gamma_i^2} \quad (21)$$

and for high SNR,

$$\sigma_{\theta_{cl,high}}^2 \approx \frac{1}{\hat{n} N_f} \sum_{i=1}^t \frac{1}{\gamma_i^2} \quad (22)$$

where t is the order of the generalized closure. Note that if we take the logarithm of Equation (23), we obtain:

$$\log \sigma_{\theta_{cl,low}}^2 \approx t \log \frac{2}{\hat{n}} - 2 \sum_{i=1}^t \log \gamma_i - \log N_f \quad (23)$$

2.4 Covariance Matrix of the Generalized Closure Phases for the Pairwise Architecture

In this section we generalize results of [Kulkarni et al. \(1991\)](#) to obtain expressions for the n-spectra covariance matrices. We will first compute the covariance between two n-spectrum phasors $\mathbf{G}_1 = \text{Re}[G_1] + j\text{Im}[G_1]$, with $E[\mathbf{G}_1] = \mathbf{g}_1$,

and $\mathbf{G}_2 = \text{Re}[G_2] + j\text{Im}[G_2]$, and $E[\mathbf{G}_2] = \mathbf{g}_2$. Let I and J denote the set of baselines in n-spectra G_1 and G_2 , respectively. Then we have:

$$\sigma(G_1, G_2^*) = \left\langle \prod_{i \in I} z_i \prod_{j \in J} z_j^* \right\rangle - \left\langle \prod_{i \in I} \langle z_i \rangle \prod_{j \in J} \langle z_j^* \rangle \right\rangle \quad (24)$$

We can then factor out the factors common to G_1 and G_2 from those which are distinct to obtain:

$$\sigma(G_1, G_2^*) = \left[\prod_{k \in I \cap J} \langle z_k z_k^* \rangle - \prod_{k \in I \cap J} \langle z_k \rangle \langle z_k^* \rangle \right] \prod_{l \in I \setminus J} \langle z_l \rangle \prod_{m \in J \setminus I} \langle z_m^* \rangle \quad (25)$$

Making the appropriate substitutions from Section 1.2, we obtain:

$$\sigma(G_1, G_2^*) = e^{2\pi j(\angle G_1 - \angle G_2)} \left[\prod_{k \in I \cap J} (\hat{n}^2 \gamma_k^2 + 2\hat{n} \delta_{z_{1,k}, z_{2,k}}) - \prod_{k \in I \cap J} \hat{n}^2 \gamma_k^2 \right] \times \prod_{l \in I \setminus J} \hat{n} \gamma_l \prod_{m \in J \setminus I} \hat{n} \gamma_m \quad (26)$$

where $\delta_{z_{1,k}, z_{2,k}} = 1$ if the common measurements are the same, and zero if they are conjugates of each other. Similarly,

$$\sigma(G_1, G_2) = e^{2\pi j(\angle G_1 + \angle G_2)} \left[\prod_{k \in I \cap J} (\hat{n}^2 \gamma_k^2 + 2\hat{n} \bar{\delta}_{z_{1,k}, z_{2,k}}) - \prod_{k \in I \cap J} \hat{n}^2 \gamma_k^2 \right] \times \prod_{l \in I \setminus J} \hat{n} \gamma_l \prod_{m \in J \setminus I} \hat{n} \gamma_m \quad (27)$$

where $\bar{\delta}_{z_{1,k}, z_{2,k}} = 1$ if the common measurements are conjugates of each other, and zero if they are the same.

We can now compute real and imaginary n-spectra covariance as:

$$\sigma(\text{Re}[G_1], \text{Re}[G_2]) = \frac{1}{2} \text{Re}[\text{Cov}(G_1, G_2^*) + \text{Cov}(G_1, G_2)] \quad (28)$$

$$\sigma(\text{Im}[G_1], \text{Re}[G_2]) = \frac{1}{2} \text{Im}[\text{Cov}(G_1, G_2^*) + \text{Cov}(G_1, G_2)] \quad (29)$$

$$\sigma(\text{Re}[G_1], \text{Im}[G_2]) = \frac{1}{2} \text{Im}[-\text{Cov}(G_1, G_2^*) + \text{Cov}(G_1, G_2)] \quad (30)$$

$$\sigma(\text{Re}[G_1], \text{Im}[G_2]) = \frac{1}{2} \text{Re}[-\text{Cov}(G_1, G_2^*) - \text{Cov}(G_1, G_2)] \quad (31)$$

Given the n-spectra covariance expression above, we can now approximate the covariance between two generalized closure phases using Taylor series approximation of the moments, which is a technique known as the *delta method* (see, e.g. [Casella & Berger \(2002\)](#)). First we define the angle function of a phasor as $\theta(x, y) = \arctan \frac{y}{x}$. The corresponding generalized closure phases are given by: $\Theta_1 = \theta(\text{Im}[G_1], \text{Re}[G_1])$ and $\Theta_2 = \theta(\text{Im}[G_2], \text{Re}[G_2])$. Applying the delta method yields the following approximation:

$$\sigma(\Theta_1, \Theta_2) \approx \left(\frac{\partial \theta}{\partial x} \Big|_{\mathbf{g}_1} \right) \left(\frac{\partial \theta}{\partial y} \Big|_{\mathbf{g}_2} \right) \sigma(Re[G_1], Im[G_2]) \quad (32)$$

$$+ \left(\frac{\partial \theta}{\partial y} \Big|_{\mathbf{g}_1} \right) \left(\frac{\partial \theta}{\partial x} \Big|_{\mathbf{g}_2} \right) \sigma(Im[G_1], Re[G_2]) \quad (33)$$

$$+ \left(\frac{\partial \theta}{\partial y} \Big|_{\mathbf{g}_1} \right) \left(\frac{\partial \theta}{\partial y} \Big|_{\mathbf{g}_2} \right) \sigma(Im[G_1], Im[G_2]) \quad (34)$$

$$+ \left(\frac{\partial \theta}{\partial x} \Big|_{\mathbf{g}_1} \right) \left(\frac{\partial \theta}{\partial x} \Big|_{\mathbf{g}_2} \right) \sigma(Re[G_1], Re[G_2]) \quad (35)$$

Evaluation of the derivatives in the expression above yields:

$$\begin{aligned} \sigma(\Theta_1, \Theta_2) \approx & \left(\frac{-Im[g_1]}{Re[g_1]^2 + Im[g_1]^2} \right) \left(\frac{Re[g_2]}{Re[g_2]^2 + Im[g_2]^2} \right) \sigma(Re[G_1], Im[G_2]) \\ & + \left(\frac{Re[g_1]}{Re[g_1]^2 + Im[g_1]^2} \right) \left(\frac{-Im[g_2]}{Re[g_2]^2 + Im[g_2]^2} \right) \sigma(Im[G_1], Re[G_2]) \\ & + \left(\frac{Re[g_1]}{Re[g_1]^2 + Im[g_1]^2} \right) \left(\frac{Re[g_2]}{Re[g_2]^2 + Im[g_2]^2} \right) \sigma(Im[G_1], Im[G_2]) \\ & + \left(\frac{-Im[g_1]}{Re[g_1]^2 + Im[g_1]^2} \right) \left(\frac{-Im[g_2]}{Re[g_2]^2 + Im[g_2]^2} \right) \sigma(Re[G_1], Re[G_2]) \end{aligned} \quad (36)$$

2.5 Covariance Matrix Approximations for the Fizeau Architecture

In the Fizeau case, Equation (9) becomes:

$$\langle zz^* \rangle = \gamma^2 n^2 + N_{ap} n \quad (37)$$

As shown in Appendix A, we can approximate the variance of a n-spectrum of order o as:

$$V_{Fizeau}(G) \approx \left[\prod_{i=1}^t (n^2 \gamma_i^2 + N_{ap} n) \right] - n^{2t} \prod_{i=1}^t \gamma_i^2 \quad (38)$$

Hence the SNR can be approximated as:

$$S_{Fizeau} \approx \frac{\sqrt{2} n^t \prod_{i=1}^t \gamma_i}{\sqrt{\left[\prod_{i=1}^t (n^2 \gamma_i^2 + N_{ap} n) \right] - n^{2t} \prod_{i=1}^t \gamma_i^2}} \quad (39)$$

Applying the same approximations in Appendix A to the covariance yields the following analogues to Equations (26)-(27)

$$\begin{aligned} \sigma(G_1, G_2^*) &= e^{2\pi j(\angle G_1 - \angle G_2)} \\ &\times \left[\prod_{k \in I \cap J} (n^2 \gamma_k^2 + N_{ap} n \delta_{z_{1,k}, z_{2,k}}) - \prod_{k \in I \cap J} n^2 \gamma_k^2 \right] \prod_{l \in I \setminus J} n \gamma_l \prod_{m \in J \setminus I} n \gamma_m \end{aligned} \quad (40)$$

and,

$$\begin{aligned} \sigma(G_1, G_2) &= e^{2\pi j(\angle G_1 + \angle G_2)} \\ &\times \left[\prod_{k \in I \cap J} (n^2 \gamma_k^2 + N_{ap} n \delta_{z_{1,k}, z_{2,k}}) - \prod_{k \in I \cap J} n^2 \gamma_k^2 \right] \times \prod_{l \in I \setminus J} n \gamma_l \prod_{m \in J \setminus I} n \gamma_m \end{aligned} \quad (41)$$

3 FOURIER PHASE RECOVERY USING THE N-SPECTRA

In this section, we briefly review the integer least-squares approach for RSC phase recovery (see e.g. [Lannes & Anterrieu \(1999\)](#), [Kurien et al. \(2016\)](#) for more comprehensive treatments), and then describe an algorithm for selection of a set of generalized closure relations of minimum total variance.

3.1 RSC Phase Recovery with Wrap-Invariant Patterns

The traditional approach to RSC reconstruction operates on the measured baseline phases (see e.g. [Arnot et al. \(1985\)](#), [Greenaway \(1994\)](#)). To illustrate the approach, let us consider an interferometer which operates at a wavelength λ with two apertures (say, i and j) separated by a vector baseline distance of \mathbf{b}_{ij} . In the absence of any optical path difference, the interference pattern formed by these two apertures encodes a sample of the object's Fourier Transform at spatial frequency $\frac{\mathbf{b}_{ij}}{\lambda}$. Let the true Fourier phase (which we will refer to as *object phase*), measured by this interference pattern be denoted as θ_{ij} . The measured phase is given by:

$$\beta_{ij} = \theta_{ij} + \phi_j - \phi_i + 2\pi e \quad (42)$$

where $\phi_j - \phi_i$ is the optical path difference between apertures j and i , and e is unknown phase wrap integer arising from the fact that interferometric phase measurements are only known modulo 2π .

Consider an interferometric array which simultaneously makes many such measurements amongst its N_{ap} apertures. Suppose that of the array's $\binom{N_{ap}}{2}$ baselines, d of them are distinct. Further suppose we have a solution set $\{\phi_i\}$ and $\{\theta_{ij}\}$ for these equations. Let \mathbf{r}_i denote the vector position of the i -th aperture. As noted by several authors (see, e.g. [Wieringa \(1992\)](#)), we can obtain another valid solution set simply by replacing each ϕ_i with $\phi_i^P = \phi_i + \mathbf{z} \cdot \mathbf{r}_i$, and each θ_{ij} with $\theta_{ij}^P = \theta_{ij} - \mathbf{z} \cdot (\mathbf{r}_j - \mathbf{r}_i)$, for arbitrary ϕ_0 and \mathbf{z} . Since the free vector \mathbf{z} is a two-parameter vector representing the inherently-ambiguous position of the image within the field-of-view and the free parameter ϕ_0 is simply a scalar piston offset, the kernel of the RSC system is three-dimensional. Therefore the RSC system contains d unknown distinct object phases and N_{ap} unknown aperture pistons, and is rank-deficient by at least 3. This implies that there are at most $(d + N_{ap} - 3)$ linearly-independent equations in the RSC system, and hence at most $N_{ap} - 3$ redundant relations can be linearly-independent. We will assume for the remainder of the paper that our array contains $N_{ap} - 3$ independent relations. **Under this assumption, we can then solve for a particular solution of this system by arbitrarily setting the value of two object phases (whose spatial**

freqencies are not co-linear) and one piston phase. This particular solution will then differ from the true solution by a phase ramp in the Fourier domain, corresponding to an image shift in the spatial domain.

Using \mathbf{M} to denote the coefficients of the equations, we can write the RSC system in compact form as:

$$\mathbf{M} \begin{bmatrix} \vec{\theta} \\ \vec{\phi} \end{bmatrix} = \beta + 2\pi\mathbf{e} \quad (43)$$

We now show how generalized closures **eliminate** the ϕ contribution to the model in Equation (43) and thereby **provide a means for Fourier phase recovery** in scenarios where fringe tracking capabilities are either **unavailable or degraded due to low SNR**. First we **define** the *interferometric graph* of an array as the directed graph whose vertices are the N_{ap} apertures in the array and edges are the $\binom{N_{ap}}{2}$ baselines connecting all vertex pairs. We also **define** the *spectral phase space* K as the span of the d columns associated with the Fourier phases, or equivalently the range of the sub-matrix \mathbf{M}_θ formed by these columns. The piston, or *aberration*, phase space L is the span of the N_{ap} columns associated with the piston phases, or equivalently the range of the sub-matrix \mathbf{M}_ϕ formed by these columns. \square

Note that the d columns spanning K are linearly-independent by virtue of having non-zero entries in mutually disjoint sets of baseline indices. Hence $\dim(K) = d$. The subspace L has dimension $N_{ap} - 1$ (Lannes & Anterrieu 1999); the constant vector forms the one-dimensional nullspace of \mathbf{M}_ϕ .

We generalize the notion of phase closure in a structured manner by defining the important concept of the *cycle space* of the interferometric graph. Given a directed graph G with a set of vertices V and edges E , the *cycle space* of the graph is the vector space of $\mathbb{Q}^{|E|}$ spanned by the incidence vectors of cycles with a (clockwise, or counter-clockwise) *orientation*. It can be shown that the dimension of the cycle space is $M + N - 1$, where $M = |E|$ and $N = |V|$.

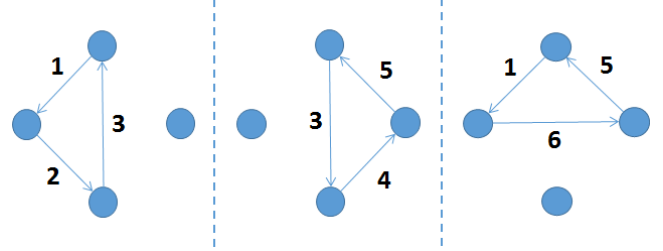
Suppose we have a basis for the cycle-space of the interferometric graph. Let us stack the elements of this basis as row vectors in a $\binom{N_{ap}-1}{2} \times \binom{N_{ap}}{2}$ matrix \mathbf{C}_{mc} , which maps baseline phase measurements to generalized closure phases. Recall from the discussion of n-spectra in Section 1 that closure relations eliminate piston differences in the measurements so that \mathbf{C}_{mc} annihilates the subspace L (see e.g. Lannes (2003)), i.e. the space spanned by the columns of \mathbf{M} corresponding to $\vec{\phi}$.

In Figure 3, we show a simple four-aperture interferometric graph and one possible cycle basis for the graph. For this particular example, we can write:

$$\mathbf{C}_{mc} = \begin{bmatrix} 1 & 1 & 1 & 0 & 0 & 0 \\ 0 & 0 & -1 & 1 & 1 & 0 \\ 1 & 0 & 0 & 0 & 1 & 1 \end{bmatrix} \quad (44)$$

where the column (i.e. baseline) indexing in the matrix follows the labeling in the Figure. Note that the final triangle cycle (i.e. the one containing baselines 2, 4, and 6, and represented by the row vector $\mathbf{w}^* := (0, 1, 0, 1, 0, -1)$), can be represented as a linear combination of the cycles in the basis: $\mathbf{w}^* = \mathbf{c}_1 + \mathbf{c}_2 - \mathbf{c}_3$, where $\{\mathbf{c}_i\}$ are the rows of \mathbf{C}_{mc}

Figure 3. One possible cycle-basis for a simple interferometric graph. Note the fourth triangle (i.e. baseline set $\{2, 4, 6\}$) can be expressed as a linear combination of the cycles shown.



While for purposes of simplicity we have chosen a cycle basis consisting exclusively of three-baseline cycles, in general the elements of a cycle basis can contain any number of edges.

As the closure relations defined by \mathbf{C}_{mc} annihilate the subspace L , we have:

$$\mathbf{C}_{mc} \mathbf{M} \begin{bmatrix} \vec{\theta} \\ \vec{\phi} \end{bmatrix} = \begin{bmatrix} \mathbf{C}_{oc} & \mathbf{0} \end{bmatrix} \begin{bmatrix} \vec{\theta} \\ \vec{\phi} \end{bmatrix} \quad (45)$$

where $\mathbf{C}_{oc} := \mathbf{C}_{mc} \mathbf{M}_\theta$, and is the mapping between object phases and closure phases.

By standard principles of linear algebra, we know that the ability to uniquely recover the set of object phases given closure phase measurements amounts to the injectivity of the matrix \mathbf{C}_{oc} , which can be verified by examining its nullspace. Let $\Delta\mathbf{r}_x$ and $\Delta\mathbf{r}_y$ denote the vectors containing the x - and y -coordinates of the baselines in an array, respectively. If the array is a valid RSC array, these columns form a basis for the two-dimensional nullspace of \mathbf{C}_{oc} . Given that the nullspace is composed of linear combinations of the array baseline vectors, which are in turn scaled versions of the array's spatial frequencies, the mapping \mathbf{C}_{oc} is injective up to a linear frequency ramp (or, equivalently, an image shift). The proof is given in Appendix B.

In addition to ensuring injectivity of the closure mapping, we must also address the difficulty arising from the fact that generalized closure phases are only known 2π . Let us define \mathbf{y}_{cl} as the observation vector of wrapped generalized closure phases, and $2\pi\mathbf{e}_{cl}$ the wrapping vector (with integer \mathbf{e}_{cl}). Our phase measurement model is then given by:

$$\mathbf{C}_{oc} \vec{\theta} = \mathbf{y}_e + \mathbf{n} \quad (46)$$

where $\mathbf{y}_e = \mathbf{y}_{cl} + 2\pi\mathbf{e}_{cl}$, and \mathbf{n} is the measurement noise, which we shall assume in this paper is predominantly due to shot noise on the focal plane.

We can now formulate the well-posed recovery of the Fourier phases as the following generalized, integer least-squares problem, which finds a vector in the range of the closure matrix at a minimum Mahalanobis distance from the actual, wrapped measurement vector:

$$\hat{\theta}_{RSC} = \operatorname{argmin}_{\mathbf{e}_{cl}, \vec{\theta}} (\mathbf{y}_e - \mathbf{C}_{oc} \vec{\theta})^T \hat{\Sigma}^{-1} (\mathbf{y}_e - \mathbf{C}_{oc} \vec{\theta}) \quad (47)$$

where $\hat{\Sigma}$ is an estimator of the covariance matrix of the phase

measurements. This estimator can be obtained by substituting estimates for the object visibilities $\{\gamma_i\}$ into the covariance expressions in the previous section. It is acknowledged that this least-squares solution is neither the optimal nor maximum-likelihood solution to the phase inference problem. For one, a Gaussian distribution on the closure phases is implicitly assumed to hold, and can only approximately hold for high-SNR closure phases. It is therefore assumed that n-spectra will be integrated for a sufficiently large number of frames for this approximation to be reliable for most, if not all, of the closure phases.

Assuming the covariance matrix estimator is not degenerate, it will admit a Cholesky-decomposition $\Sigma = \mathbf{B}\mathbf{B}^T$. Equation (47) is then equivalent to searching for vectors \mathbf{e} which minimize the projection of a whitened measurement $\mathbf{B}^{-1}\mathbf{y}_e$ onto the subspace defined by $\text{ker}((\mathbf{B}^{-1}\mathbf{C}_{oc})^T)$. Specifically we seek to minimize:

$$f(\mathbf{e}) = \|\mathbf{P}_\Sigma \mathbf{B}^{-1}(\mathbf{y}_{cl} + 2\pi\mathbf{e}_{cl})\|^2 \quad (48)$$

where \mathbf{P}_Σ is a matrix representing the orthogonal projection from \mathbb{R}^n onto $\text{ker}((\mathbf{B}^{-1}\mathbf{C}_{oc})^T)$.

Letting $\mathbf{e}'_{cl} = -\mathbf{e}_{cl}$, we can rewrite the above objective function as:

$$f(\mathbf{e}') = \|\mathbf{P}_\Sigma \mathbf{B}^{-1}(\mathbf{y}_{cl} - 2\pi\mathbf{e}'_{cl})\|^2 = \|\mathbf{P}_\Sigma \mathbf{B}^{-1}\mathbf{y}_{cl} - 2\pi\mathbf{P}_\Sigma \mathbf{B}^{-1}\mathbf{e}'_{cl}\|^2 \quad (49)$$

This optimization problem is equivalent to the so-called *closest vector problem* (CVP) in the theory of lattices. The connection of interferometric phase-unwrapping with the CVP problem was, to the best of our knowledge, first explored in [Lannes & Anterrieu \(1999\)](#). In this paper, the authors formulate an analogous minimization problem for the raw baseline measurements.

We will define a lattice $\mathbf{L}(\mathbb{Z}^n)$ as the set of points generated by integer combinations of the column vectors of a matrix \mathbf{L} . Letting $\tilde{\mathbf{P}} = \mathbf{P}_\Sigma \mathbf{B}^{-1}$ and factoring 2π , our optimization problem then amounts to the following: Find the lattice point in $\tilde{\mathbf{P}}(\mathbb{Z}^n)$ which is closest to $\tilde{\mathbf{P}}\mathbf{y}_{cl}/(2\pi)$. A compact representation of the lattice Γ is given by:

$$\Gamma = \left\{ \sum_{i=1}^{m \leq n-(d+N-3)} a_i \mathbf{v}_i \mid \forall a_i \in \mathbb{Z} \right\} \quad (50)$$

where $\{\mathbf{v}_i\}$ are linearly-independent and together form a *basis* of the lattice. Given the lattice basis, several algorithms exist for finding the closest lattice point to a specified vector. A popular class of algorithms, known as the Sphere-Decoding algorithms, are efficient searches for the closest lattice point within a hypersphere of a certain radius centered on the input vector (see e.g. [Agrell et al. \(2002\)](#)). For the simulations in this paper, we instead use the lower-complexity Babai Nearest Plane (Babai-NP) algorithm ([Babai 1986](#)). For lattice bases which are nearly orthogonal (such as those we use for our simulations), this algorithm offers reliable, albeit not guaranteed, performance in practice.

Suppose we have found a basis for the lattice $\tilde{\mathbf{P}}(\mathbb{Z}^n)$, and we have solved the Closest Vector Problem for a given closure vector \mathbf{y}_{cl} . Let \mathbf{b}^* be the output of the Babai Nearest Plane Algorithm - i.e. it is the lattice point which is the

closest to \mathbf{y}_{cl} .⁴ We now seek to solve for the wrap vector corresponding to this lattice point, i.e. we seek a solution to:

$$\mathbf{b}^* = \tilde{\mathbf{P}}\hat{\mathbf{e}} \quad (51)$$

Note that $\tilde{\mathbf{P}}$ is a projection matrix and thus not full-rank, and therefore there will be infinitely-many solutions to this equation. Indeed our solution \mathbf{y}_{cl}^* is correct only to within an integer vector \mathbf{e}_{resid} in the range of \mathbf{C}_{oc} . Hence there is a fundamental ambiguity that needs to be addressed. Once the measurement vector is unwrapped, there are various ways to solve the RSC system which respect the presence of a residual ambiguity \mathbf{e}_{resid} described above. Following standard least-squares principles, we first compute via projection the vector $\mathbf{y}_{cl,im(C)}^*$ in $im(\mathbf{C}_{oc})$ closest (in Mahalanobis distance) to the unwrapped measurement vector, i.e.

$$\mathbf{y}_{cl,im(C)}^* = \mathbf{B}^{-1}(\mathbf{I} - \mathbf{P}_\Sigma)\mathbf{B}\mathbf{y}_{cl}^* \quad (52)$$

Per the first method ([Lannes 2003](#)), we can compute the Smith Normal Form (SNF) ([Smith 1861](#)) of \mathbf{C}_{oc} . This matrix decomposition described in the following Theorem:

Theorem 3.1 (Smith Normal Form) ([Smith 1861](#)): Let \mathbf{A} be a nonzero $m \times n$ integer matrix with rank r . There exist integer and unimodular⁵ (and thus invertible) matrices $m \times m$ and $n \times n$ matrices \mathbf{U} and \mathbf{V} respectively such that the matrix product $\mathbf{D} = \mathbf{U}\mathbf{A}\mathbf{V}$ is a diagonal matrix whose diagonal entries \mathbf{D}_{ii} (the so-called *elementary divisors*) are non-zero integers for $i \leq r$, and zero for $i > r$. Moreover, the matrices \mathbf{U} {and respectively, the matrix \mathbf{V} } represent the row {and column} operations which zeroize \mathbf{A} below {and above} the diagonal. \square

Let us compute the Smith Normal Form (SNF) $\{\mathbf{U}, \mathbf{D}, \mathbf{V}\}$ of our matrix \mathbf{C}_{oc} , and set $\mathbf{U}_C = \mathbf{U}^{-1}$, $\mathbf{D}_C = \mathbf{D}$, and $\mathbf{V}_C = \mathbf{V}^{-1}$.

$$\mathbf{C}_{oc} = \mathbf{U}_C \mathbf{D}_C \mathbf{V}_C \quad (53)$$

A valid RSC solution can then be obtained by evaluating:

$$\hat{\theta}_{RSC} = \mathbf{V}_C^{-1} \mathbf{D}_C^+ \mathbf{U}_C^{-1} \mathbf{y}_{cl,im(C)}^* \quad (54)$$

where \mathbf{D}_C^+ denotes the pseudo-inverse of \mathbf{D} .

The effect of the residual ambiguity vector \mathbf{e}_{resid} on this solution requires careful consideration. Note that the resulting wrap-induced error in this solution is given by:

$$2\pi\mathbf{e}_{RSC} = 2\pi\mathbf{V}_C^{-1} \mathbf{D}_C^+ \mathbf{U}_C^{-1} \mathbf{e}_{resid} \quad (55)$$

Since the matrices \mathbf{U}_C and \mathbf{V}_C are unimodular, they are

⁴ It is well-known that the performance of the Babai algorithm and other CVP algorithms is improved when the lattice basis is reduced to one which has short and nearly-orthogonal vectors. We used the LLL algorithm implementation due to [Zhou \(2014\)](#) in our simulations.

⁵ A unimodular matrix is a square integer matrix whose determinant is ± 1

invertible over the integers. If all the elementary divisors in \mathbf{D}_C are equal to 1, then \mathbf{D}_C^+ will also be integral, and hence \mathbf{e}_{RSC} will be integral. This in turn guarantees that the final error in the Fourier phase will be $\mathbf{0} \bmod 2\pi$, i.e. that the RSC solution $\hat{\theta}_{RSC}$ is wrap-invariant. We hence refer to the mapping \mathbf{C}_{oc} as a *wrap-invariant* closure mapping. In Kurien et al. (2016), it was observed that this condition can be violated by RSC patterns which are not wrap-invariant. Conversely, we have observed that with wrap-invariant patterns, the closure mappings associated with the cycle bases that we will consider in this paper (i.e. fundamental cycle bases and minimum cycle bases) are also typically wrap-invariant in practice.

As it turns out, for such wrap-invariant mappings, the inverse problem in Equation (46) can be solved reliably even without the Smith Normal Form; it is sufficient to find any unimodular r -by- r sub-matrix $\tilde{\mathbf{C}}$ of \mathbf{C}_{oc} and solve the associated smaller system in Equation (56) to obtain a valid solution. Recall that for valid RSC arrays \mathbf{C}_{oc} will have $r+2$ columns and hence in this approach, two (non-collinear) object phases are implicitly set to zero. This implicit selection then fixes the fundamentally-ambiguous translation of the scene discussed at the beginning of the section.

$$\tilde{\theta} = \tilde{\mathbf{C}}^{-1} \mathbf{y}_{cl,im(C)}^* \quad (56)$$

Since $\tilde{\mathbf{C}}$ is unimodular, $\tilde{\mathbf{C}}^{-1}$ will have solely integral entries so that the resulting wrap error $\tilde{\mathbf{C}}^{-1} \mathbf{e}_{resid} = \mathbf{0} \bmod 2\pi$. Assuming the measured phase has been correctly unwrapped, the solution in Equation (56) amounts to a so-called *basic solution* of our generalized least-squares problem. We then have the following expression for the error covariance matrix for the estimator $\hat{\theta}_{RSC}$ (Kay 1993).

$$\Sigma_{basic} = (\tilde{\mathbf{C}}^T \Sigma^{-1} \tilde{\mathbf{C}})^{-1} \quad (57)$$

The basic solutions belong to the countably-infinite set of solutions to Equation (46). It turns out, somewhat surprisingly, that *any* particular solution within this set can be reliably limited to a mere image shift for patterns that are wrap-invariant. The complete set is given by:

$$\theta_\sigma = \mathbf{C}_{oc}^+ \mathbf{y}_{cl,im(C)}^* + \theta_0 \quad (58)$$

where θ_0 is any vector in the nullspace of \mathbf{C}_{oc} , and \mathbf{C}_{oc}^+ denotes the pseudo-inverse of \mathbf{C}_{oc} . The pseudo-inverse can be computed using the Singular-Value-Decomposition (SVD) of \mathbf{C}_{oc} , which is given by:

$$\mathbf{C}_{oc} = \mathbf{U}_\sigma \Sigma_\sigma \mathbf{V}_\sigma \quad (59)$$

where \mathbf{U}_σ and \mathbf{V}_σ are $\binom{N_{ap}}{2} \times \binom{N_{ap}}{2}$ and $d \times d$ orthogonal matrices, respectively. Σ_σ is a $\binom{N_{ap}}{2} \times d$ diagonal matrix with r non-zero diagonal entries (the so-called *singular values* of \mathbf{C}_{oc}), where $r = \text{rank}(\mathbf{C}_{oc}) = d - 2$.

The Moore-Penrose pseudo-inverse is then given by (Bretschler 2001):

$$\mathbf{C}_{oc}^+ = \mathbf{U}_\sigma \Sigma_\sigma^+ \mathbf{V}_\sigma^T \quad (60)$$

where Σ_σ^+ is a diagonal matrix whose r non-zero diagonal

entries are the reciprocals of the corresponding non-zero entries in Σ_σ .

In our companion paper (Kurien et al. 2016), we show that the effect of wrapping on the RSC pseudo-inverse solution to Equation (43) can be reliably limited to an image shift for wrap-invariant patterns. An analogous result applies to closure-based RSC imaging:

Proposition 3.2: If a pattern is wrap-invariant, the error induced by wrapping of the (generalized) closure phases can be limited to an image shift.

Proof: See Appendix C \square

The covariance of elements in the pseudo-inverse solution can be expressed as (Montgomery et al. 2006):

$$\Sigma_{pinv} = \hat{\mathbf{V}}_\sigma^T \Sigma_+^2 \hat{\mathbf{V}}_\sigma \quad (61)$$

where $\hat{\mathbf{V}}_\sigma$ is obtained by omitting the final 2 columns of \mathbf{V}_σ which form a basis for the nullspace of \mathbf{C}_{oc} .

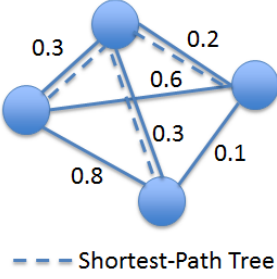
3.2 Selection of the N-Spectra

In this section, we describe a strategy for obtaining a near-optimal linearly-independent set of generalized closure phases. This strategy is founded on the notion of *minimum cycle basis* from graph theory, which is defined as follows. Let each edge of the graph be assigned a positive weight c_k , and the weight of a cycle be defined as the sum of the weights of its constituent cycles. We can then ask for the set of linearly-independent oriented cycles which spans the cycle space and has minimum total weight. We call such a set the *minimum cycle basis* of a directed graph G .

The canonical method for finding a minimum cycle basis is known as the *greedy algorithm*, which is defined as follows. Consider a vector space V , a set of vectors which span V , and a corresponding set of weights for each of these vectors. A basis of minimum total weight can be found by first sorting the vectors in decreasing order of weight, and then selecting vectors for the basis in this order if and only if they are linearly-independent of previous selections. It can be shown that this strategy is guaranteed to output a minimum cycle basis. (Gross & Yellen 2006)

We can find a set of linearly-independent closure relations of minimum total variance by employing the greedy algorithm on the set S of all possible closure relations. However, this set is equivalent to the set of all possible cyclic permutations, which becomes enormous for arrays of large size. Fortunately, in an extension of a result due to Horton (1987) for undirected graphs, Liebchen & Rizzi (2005) showed that the elements of the minimum cycle basis of a directed graph could be found among a special (and much smaller) subset of S known as the *Horton cycles*.

To define the *Horton cycle*, we must first introduce the concept of *shortest path tree* for those readers who may not familiar with it. The shortest path tree of a graph G with respect to a node A is the spanning tree which connects node A to each other node in G via a path of minimum weight. Figure 4 gives a simple example of a shortest path tree for an interferometric graph in which the top-most node is the root. The construction of shortest path trees is a well-studied problem in graph theory (see e.g. Gross & Yellen (2006)) which is typically solved using a

Figure 4. A shortest path tree

shortest-path routine such as Dijkstra's Algorithm (Dijkstra 1959).

Given the shortest path tree T originating from an arbitrary node A , a Horton cycle is a cycle formed by connecting the endpoints of any two branches of T . As it turns out, all elements of the minimum-cycle-basis are Horton cycles. Therefore in searching for the minimum-cycle-basis, it suffices to search the Horton cycles. **A proof of this result is given in Liebchen & Rizzi (2005).**

We now leverage this fundamental result from graph theory to develop a practical method for selecting a robust set of atmosphere-invariants. Specifically, we seek a decomposition of the weight of a cycle into the weights of its constituent edges (i.e. baselines). As the following Propositions show, at the extreme low- and high-SNR limits, the n-spectrum variance does indeed allow such a decoupling.

Proposition 3.3 (Low-SNR Decoupling Approximation): In the low-SNR limit, the logarithm of the total variance of any cycle is given (up to a global additive constant) by the sum of the costs assigned to each baseline in the cycle, where the cost of a baseline k with visibility γ_k is given by: $c_k = \log \frac{2}{n} - 2 \log \gamma_k$.

Proof: This can be seen by re-writing the low-SNR approximation in Equation (23) as:

$$\log \sigma_{\theta_{cl,low}}^2 \approx \sum_{i=1}^t \log \frac{2}{n} - 2 \log \gamma_i + C \quad (62)$$

where $C = \log N_f$ is a constant with respect to both visibility and flux and therefore irrelevant for the purposes of closure selection. \square

Proposition 3.4 (High-SNR Decoupling Approximation): In the high-SNR limit, the total variance of any cycle is given (up to a global scaling factor) by the sum of the costs assigned to each baseline in the cycle, where the cost of a baseline i with visibility γ_i is given by: $c_i = \frac{1}{\gamma_i^2}$.

Proof: This follows directly from the high-SNR approximation in Equation (22). \square

Based on the Propositions above, we now have a way to construct a set of linearly-independent generalized closures of minimum variance at the low- and high- SNR extremes. As demonstrated in the next section, even at moderate flux-levels where these approximations lack precision, this new closure selection method can yield significant improvements over traditional closure imaging restricted to baseline triangles. To estimate the scaling of the computational cost of the method, recall that the greedy algorithm is run on the set of Horton cycles. Since there are N_{ap} shortest-path

trees, each rooted at a distinct aperture, and $m - (N_{ap} - 1)$ cycles in each of these trees, the total number of Horton cycles is $O(mN_{ap})$. Since $m = O(N_{ap}^2)$, we see that the algorithm is $O(N_{ap}^3)$, which is the same complexity as if the greedy algorithm were run on an exhaustive listing of all $\binom{N_{ap}}{3}$ three-baseline closures.

3.3 Complete Algorithm

We are now in a position to synthesize the techniques developed in previous sections into an algorithm for RSC imaging using generalized closures. Recall that closure selection relies on estimates of the baseline visibilities $\{\gamma_i\}$. These estimates can be derived for the pairwise case by solving Equation (9) for γ to yield:

$$\gamma_i = \frac{\sqrt{\langle zz^* \rangle - 2\hat{n}}}{\hat{n}} \quad (63)$$

Similarly, for the Fizeau case, we can solve Equation (37) to obtain:

$$\gamma_i = \frac{\sqrt{\langle zz^* \rangle - N_{ap}n}}{n} \quad (64)$$

We can now combine corresponding estimates of the Fourier phases and visibilities to form Fourier phasor estimates $\hat{\mathbf{y}}$, which are known as *complex visibilities*. To estimate the image coefficients $\hat{\mathbf{x}}$ from these complex visibilities, we must apply a deconvolution algorithm. Based on the demonstrated effectiveness of recent compressed sensing techniques, we choose the sparse recovery technique known as **Total Variation Minimization** (Rudin et al. 1992) to perform this deconvolution. Namely our image estimate is given by:

$$\hat{\mathbf{x}} = \arg \min_{\alpha} \|\alpha\|_{TV} \text{ subject to: } \|\mathbf{F}\alpha - \hat{\mathbf{y}}\|_2 \leq \epsilon \quad (65)$$

where \mathbf{F} is a partial Fourier matrix whose rows are vectorized representations of the 2D sinusoids associated with the array's measured spatial frequencies. **For the image reconstructions conducted below, we used the NESTA software package (Becker et al. 2011) to perform this regularization.**

Algorithm 1 provides the complete set of steps we have discussed.

4 ALGORITHM PERFORMANCE

In this Section, we present the results of application of Algorithm 1 to a simulated scenario of imaging a structured object space.

4.1 Sensitivity Limits

A useful benchmark for our results is provided by the Cramer-Rao Lower Bound (CRLB) for interferometric phase

Algorithm 1 RSC Image Reconstruction Algorithm

1. Estimate visibilities γ_i (c.f. Equations (63)-(64))
- 2 Select n-spectra relations via minimum cycle basis
- 2.1 Choose decoupling approximation according to SNR regime (c.f. Proposition 3.3 or 3.4)
- 2.2 Assign baseline edge weights accordingly
- 2.3 Enumerate the Horton cycles of the interferometric graph
- 2.4 Execute greedy algorithm on set of Horton cycles to find minimum-variance set of $m - (N_{ap} - 1)$ n-spectra
3. Average the selected n-spectra
4. Unwrap the generalized closure phases corresponding to these n-spectra (c.f. Section 3.1)
5. Solve generalized least-squares problem with unwrapped generalized closures
6. De-convolve the estimated complex visibilities to reconstruct image using the regularization in Equation (65) or other regularization technique

estimation in the absence of atmospheric turbulence. We begin by defining our fringe measurement model in the standard way (see, e.g. [Gordon, J. A. & Buscher, D. F. \(2012\)](#)):

$$\mathbf{p} = \mathbf{Q} \begin{bmatrix} \mathbf{x}_{cv} \\ \mathbf{y}_{cv} \end{bmatrix} + \eta \mathbf{1} \quad (66)$$

where \mathbf{p} is the vector of pixel counts, \mathbf{x}_{cv} , and \mathbf{y}_{cv} are respectively the $\binom{N_{ap}}{2}$ real and imaginary components of the complex-visibility components, respectively, \mathbf{Q} is the matrix mapping the real and imaginary parts of the complex visibilities to pixels on the focal plane (often called the visibility-to-pixel matrix *V2PM* in the literature), $\mathbf{1}$ is the all-ones vector, and η is a constant scalar whose value is proportional to the overall brightness of the target. Note that rows of \mathbf{Q} are the sinusoidal functions associated with each fringe generated by the beam combiner.

Leveraging analysis by [Zmaidzinas \(2003\)](#), we can compute the Fisher-Information Matrix (FIM) for interferometric estimation with a Fizeau beam-combiner as:

$$\mathbf{I}_{\mathbf{x}_{cv}, \mathbf{y}_{cv}} = (\mathbf{Q}^T \Lambda_{fp}^{-1} \mathbf{Q})^{-1} \quad (67)$$

where Λ_{fp} is a diagonal matrix whose diagonal entries are the expected values of the photon counts at each detector in the array.

The CRLB for the covariance of these vector parameters is then given by:

$$\mathbf{C}_{\mathbf{x}_{cv}, \mathbf{y}_{cv}} - \mathbf{I}_{\mathbf{x}_{cv}, \mathbf{y}_{cv}}^{-1} \geq \mathbf{0} \quad (68)$$

where the notation \geq in this context means that the matrix difference on the left-hand side is positive-semidefinite.

The above bound applies to single-frame fringe phasor estimation for a non-redundant array. Since we are instead evaluating phase estimation schemes for a redundant array given multiple frames of data, we must incorporate these transformations into the bound ([Kay 1993](#)). Namely, for a redundant array, the parameter vector must be shortened to the d distinct complex-visibility phasors $\mathbf{x}_{cv,d} + (1j)\mathbf{y}_{cv,d}$. Let us define the vector $\mathbf{z}_{cv,d}$ as the concatenation of $\mathbf{x}_{cv,d}$ and $\mathbf{y}_{cv,d}$. The fringe model is then given by: $\mathbf{p} = \mathbf{QRz}_{cv,d}$, where \mathbf{R} is a $2\binom{N_{ap}}{2} \times 2d$ matrix mapping the real and imagi-

nary parts of the distinct complex visibilities to those of the $2\binom{N_{ap}}{2}$ generated fringes. The FIM then becomes:

$$\mathbf{I}_{\mathbf{z}_{cv,d}} = (\mathbf{R}^T \mathbf{Q}^T \Lambda_{fp}^{-1} \mathbf{QR})^{-1} \quad (69)$$

Defining the function $g_\theta = \arctan \frac{y_{cv,d}}{x_{cv,d}}$, the CRLB for the phase covariance matrix \mathbf{C}_θ can be expressed as:

$$\mathbf{C}_\theta - \frac{1}{N_{frames}} \frac{\partial \mathbf{g}_\theta(\mathbf{z}_{cv,d})}{\partial \mathbf{z}_{cv,d}} \mathbf{I}_{\mathbf{z}_{cv,d}}^{-1} \frac{\partial \mathbf{g}_\theta(\mathbf{z}_{cv,d})^T}{\partial \mathbf{z}_{cv,d}} \geq \mathbf{0} \quad (70)$$

where $\frac{\partial \mathbf{g}_\theta(\mathbf{z}_{cv,d})}{\partial \mathbf{z}_{cv,d}}$ is the Jacobian matrix of the distinct Fourier phases with respect to the distinct complex-visibility phasors.

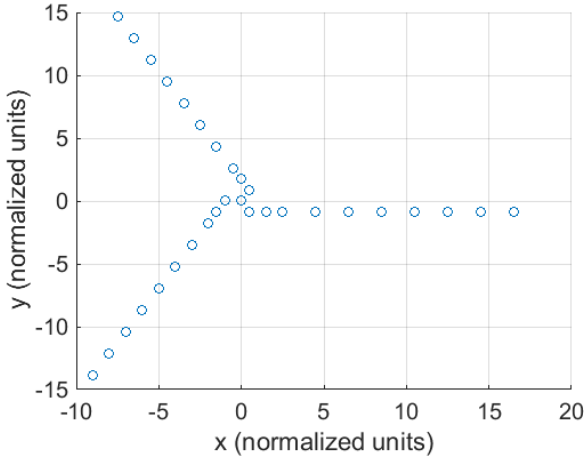
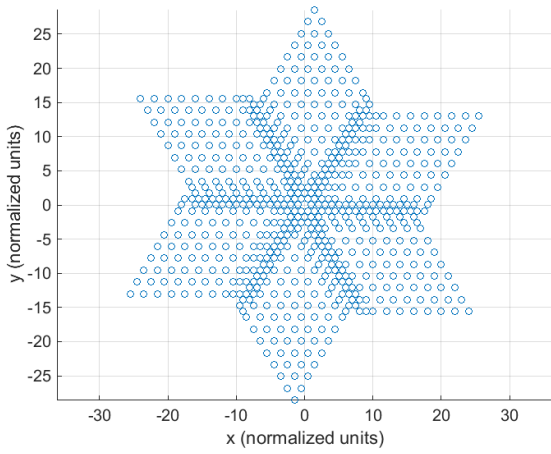
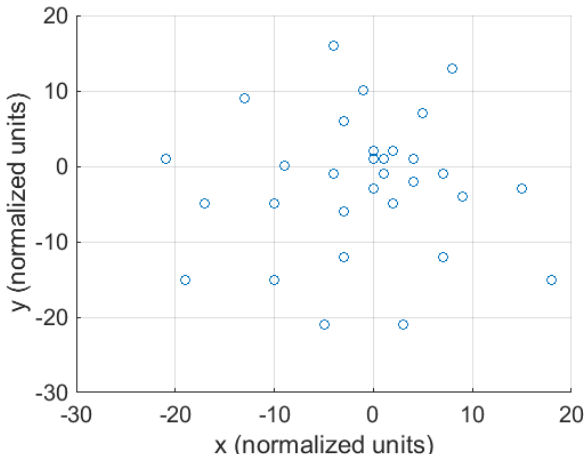
Since the left-hand-side of Inequality (70) is positive semi-definite (PSD), and the diagonal entries of a PSD matrix must be non-negative, we arrive at the following useful bound for the variance of the estimated phases:

$$var(\theta_i) \geq \frac{1}{N_{frames}} \left[\frac{\partial \mathbf{g}_\theta(\mathbf{z}_{cv,d})}{\partial \mathbf{z}_{cv,d}} \mathbf{I}_{\mathbf{z}_{cv,d}}^{-1} \frac{\partial \mathbf{g}_\theta(\mathbf{z}_{cv,d})^T}{\partial \mathbf{z}_{cv,d}} \right]_{ii} \quad (71)$$

4.2 Simulation

In this section, we provide Algorithm 1 simulation results for both interferometric architectures. For these simulations we used an RSC pattern of the Y-pattern type as shown in Figure 5. The corresponding UV-sampling for this pattern is displayed in Figure 6. To prevent aliasing on the simulated focal plane, this aperture pattern was mapped onto the Golay non-redundant pattern ([Golay 1970](#)) shown in Figure 7 for fringe generation; the model emulates the redundant-to-non-redundant pupil remapping technique developed by [Perrin et al. \(2006\)](#) and described in the Introduction. Our simulation assumed Poisson-distributed shot-noise and idealized detectors with zero read noise, and so is representative of a shot-noise-dominated scenario. The target selected was NASA's Cloud-Aerosol Lidar and Infrared Pathfinder Satellite Observations (CALIPSO) satellite for which the *truth* image ([Hill 2008](#)) is shown in Figure 8, as well as a reference image of the same at the resolution attainable by the pattern. Two flux levels (2000 photoelectrons/aperture/frame, and 500 photoelectrons/aperture/frame) were considered for these simulations. Comparative error analysis using Equation (57) showed a lower predicted RMS phase error for the decoupling approximation in **Proposition 3.3 than that in Proposition 3.4**, and hence the former was chosen in Algorithm 1. Bispectra and n-spectra were integrated for 50,000 frames, which corresponds approximately to an 8-minute observation time if we assume a typical frame duration of 10 msec. An implementation of the Bellman-Ford-Moore shortest-path algorithm ([O'Connor 2012](#)) was used to generate a minimum cycle basis as per Algorithm 1.

To show the potential impact of generalizing the closure phase notion, Algorithm 1 was compared with an analogous algorithm which instead used the minimum-variance set of $\binom{N_{ap}-1}{2}$ independent standard (i.e. three-baseline) closure phases. This minimum set was generated via application

Figure 5. RSC aperture pattern used in simulation**Figure 6.** UV-sampling for RSC pattern**Figure 7.** Golay non-redundant beam-combiner pattern

of the greedy algorithm described above to the set of all $\binom{N_{ap}-1}{2}$.

Numerical results for the pairwise and Fizeau architectures in the higher flux scenario are shown in Figures 9 and 10, respectively. In these plots, the RMS Fourier-phase errors for 10 independent simulation trials are plotted as a function of their corresponding visibilities for the basic solution. Median-filtered versions of the predicted standard errors based on Equations (57) and (61) are also shown for both basic and pseudo-inverse solutions, respectively.⁶

As expected, the Fizeau architecture proves to be more sensitive than the Pairwise architecture, which corroborates analysis by Zmuidzinas (2003). Figures 11 and 12 respectively show Fizeau performance for the higher flux scenario at a shorter integration time (1000 frames), and for the lower flux scenario at the long integration time (50,000 frames). Note that the use of independent generalized closure phases according to Algorithm 1 outperforms the analogous scheme in which only standard closures are used; the root-mean-squared (RMS) errors are noticeably lower for the former.

It is interesting to examine performance relative to the CRLB described in Section 5.1. Recall that our CRLB is an *atmosphere-oracle* bound and hence it should bound phase estimation accuracy for the case of a stationary fringe averaged over many frames. The variance of such an estimator can be easily calculated by leveraging the analysis in Section 2. Namely the pseudovariance of the phasor is given by applying Equation (37) after averaging, so that SNR of the averaged fringe phasor $\bar{\mathbf{z}}$ is given by:

$$\sigma_{\bar{\mathbf{z}}}^2 = \frac{1}{SNR_{\bar{\mathbf{z}}}} = \frac{\sigma_{\mathbf{z}}^2}{\|E[\bar{\mathbf{z}}]\|^2} = \frac{N_{ap}}{2N_{frames}ny^2} \quad (72)$$

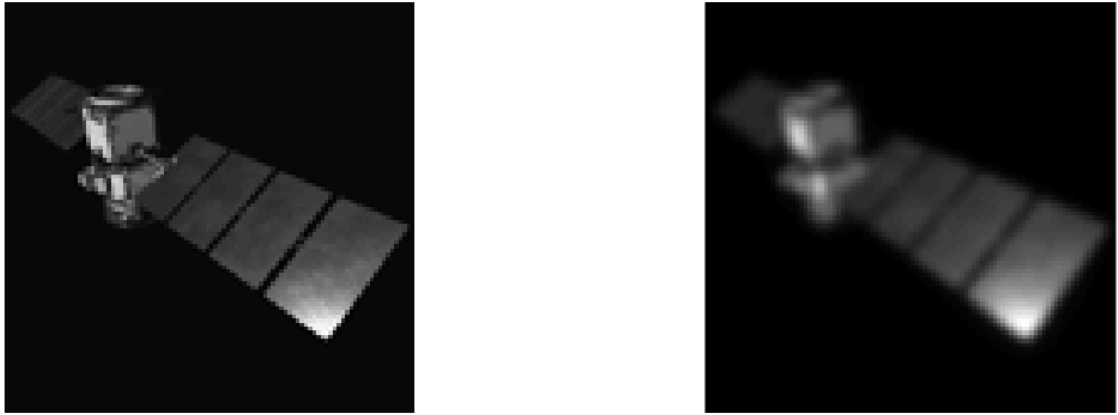
We compute the predicted phase RMS for the atmosphere-oracle by taking the square-root of this expression, and add it to the plots. From the plots, we see that CRLB is virtually identical to this expression, except for isolated dips in the CRLB. These dips correspond to the redundant baselines, which as expected, admit increased phase sensitivity due to their multiplicity.

In the higher-flux scenario ($n = 2000$), our algorithm's phase-estimation performance is within a factor of 2 from the CRLB for the vast majority of sampled visibilities. As the flux drops to $n = 500$, the performance begins to diverge from the CRLB as the closure phase variance leaves the regime described by Equation (22) and enters the regime described by Equation (21). That is, the variance is no longer accurately modeled simply by a linear combination of the individual phase variances of the form in Equation (72); rather it becomes inversely-proportional to the product of the squared-visibilities. The rapid decrease in fidelity of the closure phase at low-SNR is well-known in interferometry (Kulkarni et al. 1991).

Sample image reconstructions are shown in Figure 13.

⁶ The actual predictions exhibit oscillations, which reflect the particular structure of our mapping between Fourier phases and GC's. For clarity we have created smoothed versions of the predicted curves by creating bins with edges at visibilities $\{5, 10, 20, 40, 80, 160, 320\} * 10^{-3}$, and displaying the median values in each bin.

Figure 8. Truth image for simulation: the CALIPSO satellite (left), and Truth image at the resolution of the interferometric pattern (right)



The reconstructions derived from generalized closures show greater fidelity to the true image than those derived from standard closures, and thereby corroborate the numerical analysis presented in the plots. To quantify relative image quality, we have used the well-known *Structural Similarity Metric* (SSIM) (Wang et al. 2004). The SSIM computation decomposes the image into blocks and calculates similarity among corresponding blocks in the test image and the reference image. It is customary to report the mean of these block-wise similarity scores, i.e. the Mean Structural Similarity Metric (MSSIM). The value of MSSIM ranges from -1 , indicating maximum perceived structural dissimilarity, and 1 , indicating perfect structural similarity (i.e. identical images). The MSSIM score for each image reconstruction is reported in its caption.

It is noteworthy that while our algorithm attempts to find a minimum-variance set of n -spectra, this set is not necessarily the optimum set for phase estimation; our algorithm does not account for the conditioning of the matrix \mathbf{C}_{oc} resulting from a particular choice of n spectra. In fact there may be some cases in which the use of traditional closures results in lower phase-estimation error due to better conditioning in the corresponding \mathbf{C}_{oc} . In practice, the decision to use traditional or generalized closures can be resolved by examining the phase errors predicted by Equation (57), for basic solutions, or Equation (61) for pseudo-inverse solutions.

4.3 Generalized Closures in Non-Linear Least Squares Approaches

This paper has proposed both novel reconstruction methodology as well as new interferometric observables. A natural question arises as to whether the advantages of the latter are retained with other, existing methodology. In particular, we consider the class of techniques which solve the non-linear least squares inference problem involving normalized bis-

pectrum phasors (Gorham et al. 1989), (Negrete-Regagnon 1996). Such approaches minimize an objective of the form:

$$\Psi = \sum_{i=1}^{N_c} \frac{\left\| e^{j\hat{\beta}_{i,cl}} - e^{j(\theta_{i1} + \theta_{i2} + \theta_{i3})} \right\|^2}{w_i^2} \quad (73)$$

where N_c is the number of closures, $\hat{\beta}_{i,cl}$ is the i -th closure phase, the θ_{i1} , θ_{i2} , and θ_{i3} are the Fourier phases associated with this closure, and w_i is a weighting factor proportional to the estimated variance of the closure measurement. Objective Ψ is clearly a continuous function and hence local minima can be reliably found with gradient-descent techniques.

While such algorithms bring the complexities involved in non-linear optimization (e.g. possible stagnation in local minima and/or slow convergence), they also feature the ability to utilize any number of closure relations. Algorithm 1 restricts attention to closure relations which form cycle bases, thereby guaranteeing well-posed Fourier phase recovery while keeping the size of the associated CVP-unwrapping problem tractable. However, as noted by Kulkarni et al. (1991), fitting to all $\binom{N_{ap}}{3}$ closures will in principle improve estimation performance when the per-frame flux is low, due to the fact that closure phases de-correlate as the flux decreases⁷. Specifically, as computed by Kulkarni et al. (1991) for traditional closures in the pairwise case, the correlation coefficient μ of two closures sharing a common baseline approaches $\frac{1}{3}$ in the high-SNR regime (i.e. for $\hat{n}\gamma^2 \gg 1$) as one would expect⁸. On the other hand, the correlation coefficient in the low-SNR regime can be accurately modeled as $\mu \approx \frac{1}{4}\gamma^4\hat{n}^2$.

To assess the phase-estimation performance provided by generalized closures relative to that using the complete

⁷ The interested reader is directed to Buscher (2015) for a detailed discussion of this issue

⁸ Here Kulkarni et al. (1991) assumes a common visibility γ among all baselines in the closure

Figure 9. Pairwise Phase Recovery Results for Flux $n = 2000$ pe/ap/frame, 50,000 frames

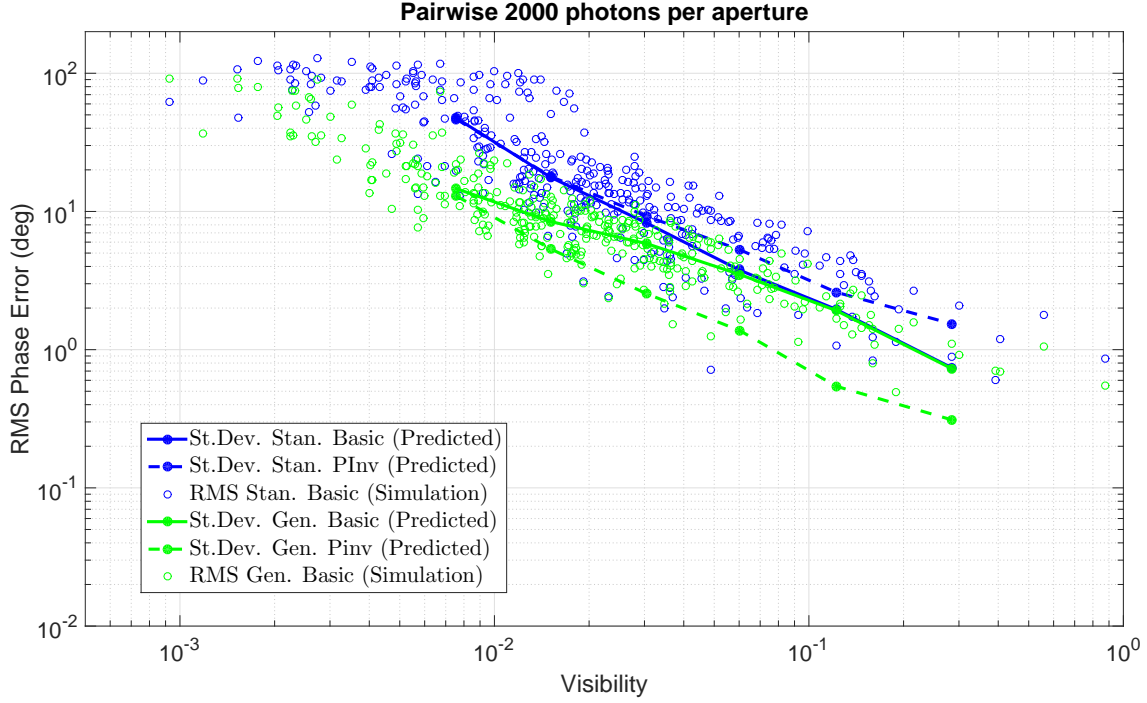


Figure 10. Fizeau Phase Recovery Results for Flux $n = 2000$ pe/ap/frame, 50,000 frames

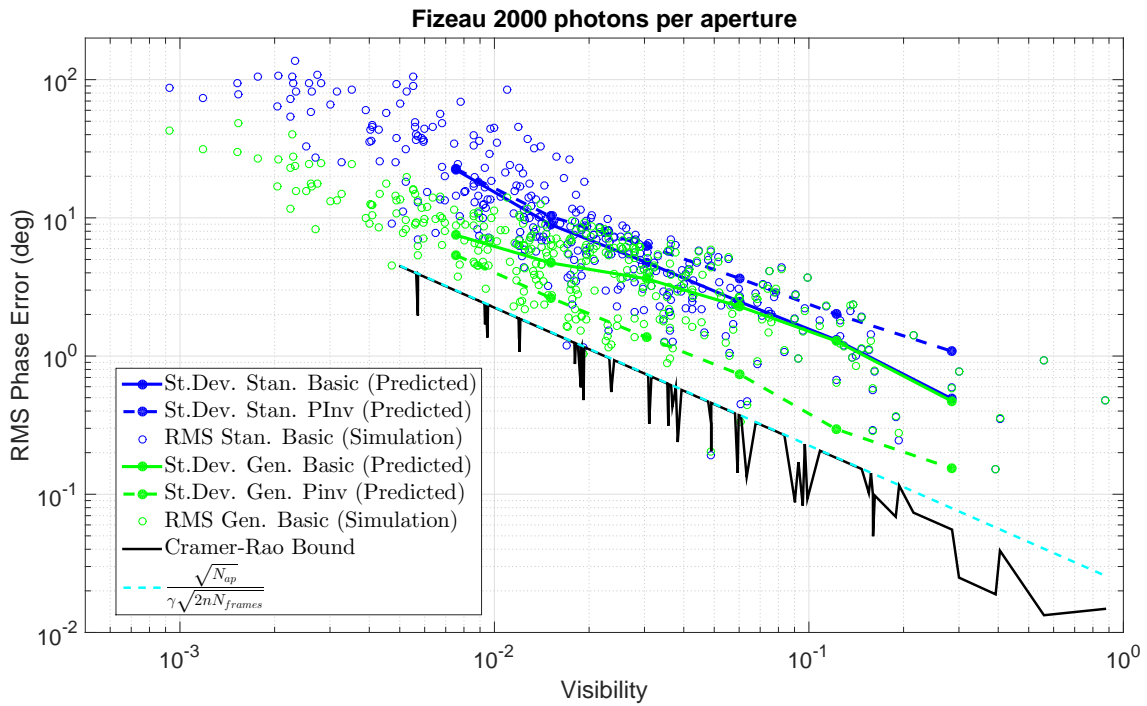


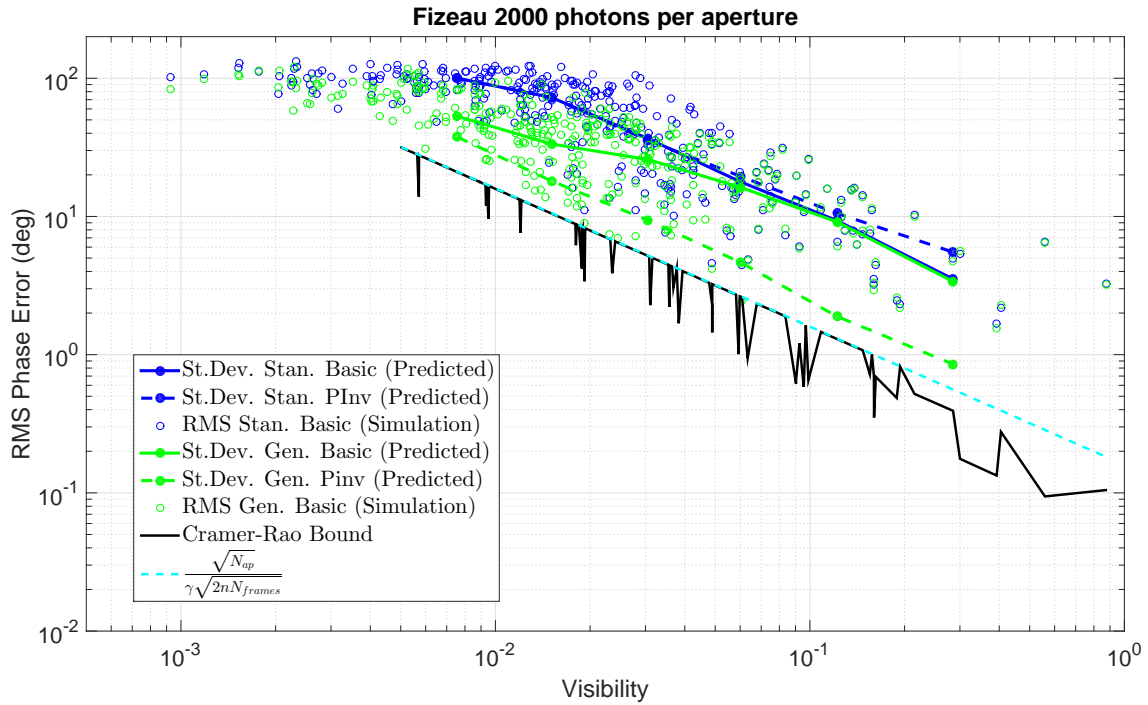
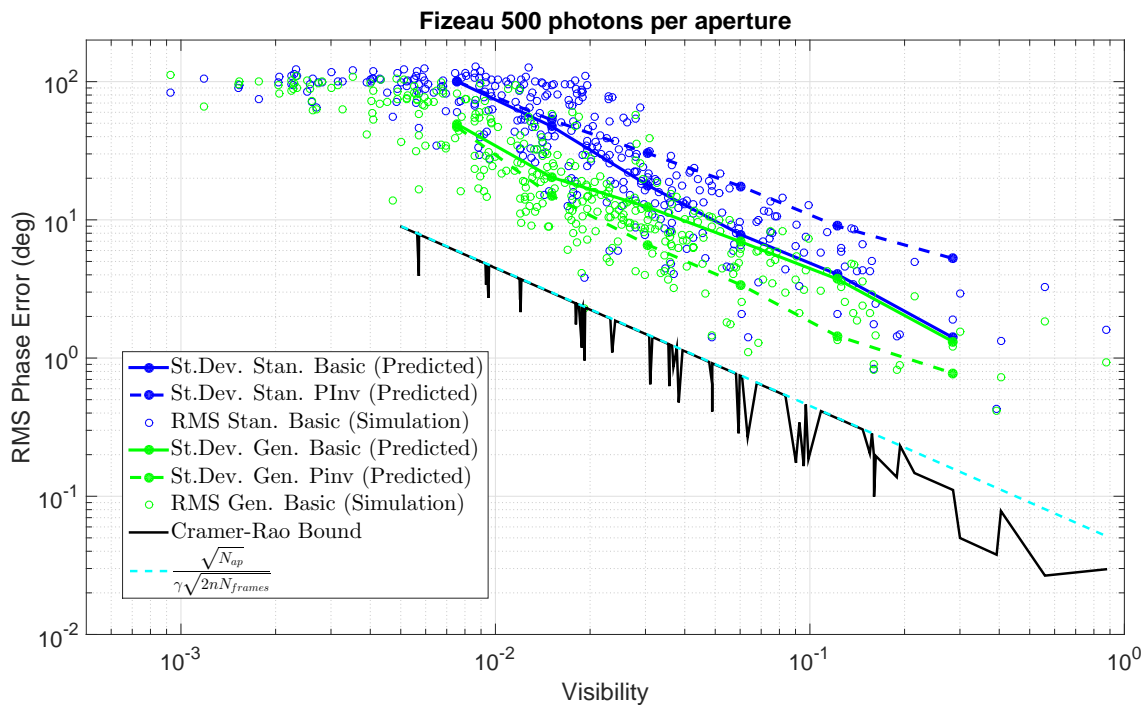
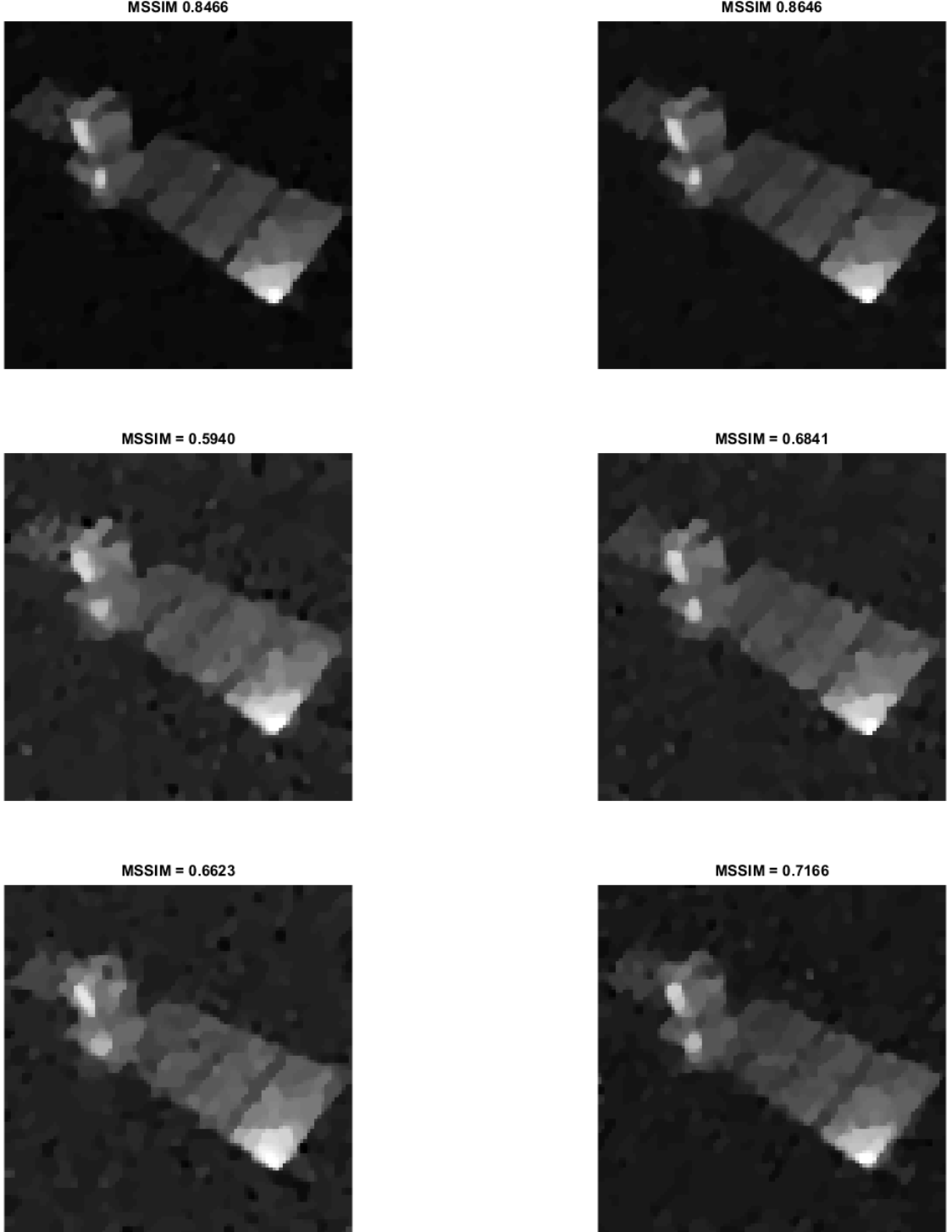
Figure 11. Fizeau Phase Recovery Results for Flux $n = 2000$ pe/ap/frame, 1000 frames**Figure 12.** Fizeau Phase Recovery Results for Flux $n = 500$ pe/ap/frame, 50,000 frames

Figure 13. Fizeau Image Reconstruction Results. The reconstructions in the left column used traditional, three-baseline observables, whereas those in the right column used generalized closures selected according to Algorithm 1. (top row) $n = 2000$ photoelectrons/aperture/frame (pe/ap/frame), 50,000 frames, (middle row) $n = 2000$ pe/ap/frame, 2000 frames, (bottom row) $n = 500$ pe/ap/frame, 50,000 frames.



set of traditional closures, we consider the algorithm developed first by Gorham et al. (1989) which works the normalized bispectrum instead of the closure phase. We used the MATLAB® non-linear least-squares solver (NLS) known as *lsqnonlin* (MATLAB 2014) to minimize the objective Ψ_2 in Equation (73). This solver obtains a quadratic approximation of the objective at each step and moves towards the minimum of this approximation, at which point another approximation is computed and the process repeats. The weights in Ψ_2 were set as in Gorham et al. (1989):

$$w_i = \frac{\hat{\sigma}_{g_i}}{\|\bar{g}_i\|} \quad (74)$$

where $\|\bar{g}_i\|$ is the magnitude of the averaged unbiased nspec-trum, and $\hat{\sigma}_{g_i}$ is the empirical standard deviation of its quadrature components.

Results of applying this solver to the lower-SNR scenario of the previous section are given in Figure 14. A single randomly-chosen initialization point was used in all cases. The top row shows reconstructions and associated convergence times for the NLS algorithm using traditional closures (left) and generalized closures selected from a minimum cycle basis (middle), respectively. The bottom row gives analogous results for the case in which all $\binom{N_{ap}}{3}$ traditional closures are used. Three snapshots at iteration counts 20, 40, and 80 are shown. Iterations after 80 resulted in negligible change to the image quality. These results suggest that generalized closures can provide at least the sensitivity of traditional closures. At the same time, they benefit from the increased convergence speed afforded by a problem size proportional to the size of cycle basis (i.e. $\propto N_{ap}^2$) as opposed to the size of the set of all closures (i.e. $\propto N_{ap}^3$). These results hence show that generalized closures can serve as more efficient sources of phase information than traditional closures.

In Figure 15, we plot phase error as a function of visibility for the NLS approach using a cycle basis of traditional closures (blue), a cycle basis of generalized closures (green), and using all $\binom{N_{ap}}{3}$ traditional closures (red). The median absolute error for 20 trials is shown in the left panel. The same median-filter that was applied to the predictions in Figures 9–12 was then applied to this raw data to produce the results in the right panel of the Figure. It is clear that the sensitivity advantage of generalizing the closure relations are retained in the NLS approach for this example.

It is noteworthy that the selection of a minimum-variance set of generalized closures involves computational overhead in the execution of the greedy algorithm. However, it is anticipated that in many cases we may be able to obtain a reliable surrogate for this set by instead forming a *fundamental cycle basis* (Liebchen & Rizzi 2005) associated with minimum-variance spanning tree of the interferometric graph. Constructing this alternate basis obviates the need for execution of the greedy algorithm; it merely requires the execution of a Minimum-weight Spanning-tree algorithm (e.g. *Prim-Jarnik Algorithm* (Prim 1957)) with each edge weight set to reciprocal of the squared visibility associated with baseline ⁹. The elements of the correspond-

ing minimum-variance spanning tree (MVST) cycle basis are then found by closing the edges of this spanning tree, which is shown in Figure 16. Indeed, many of the Horton cycles comprising the minimum cycle basis computed for this example pattern and scenario are also members of the MVST basis. Not surprisingly, the reconstruction with this basis approaches the quality of that for the minimum-cycle-basis set (c.f. middle and bottom images in left column of Figure 14). Moreover the median absolute phase error for this approach, which is shown in cyan in the right panel of Figure 15, is very similar to that observed with the Minimum Cycle Basis.

While the analysis of Kulkarni et al. (1991) revealed the advantage of supplementing a cycle basis with additional traditional closures in the pairwise case, this advantage should in principle extend to the case of generalized closure phases in the Fizeau architecture. Our CRLB comparison above (i.e. Figures 10 and 11) confirms that there is limited scope for improvement in the regime $\frac{n}{N_{ap}} \approx 60$. In the regime explored in the lower-SNR scenario (see Figure 12), however, there is certainly a CRLB-gap which may be closed with appropriate selection of supplementary generalized closures. We leave the development of algorithms to perform such a selection efficiently for future work.

5 CONCLUSION

In this paper, we have developed a novel method for interferometric imaging which employs RSC techniques and a generalized notion of bispectrum observable (the *n-spectrum*). We have established that phase estimation from these observables is well-posed for valid RSC arrays. We have also provided a fast algorithm for selection of a minimum-variance set of these observables, which is based on the concept of *minimum cycle basis* in graph theory. Then, leveraging the lattice-theory problem formulation first proposed by Lannes & Anterrieu (1999) for unwrapping of the closure phases, as well as techniques from sparse recovery for image reconstruction in the presence of Fourier undersampling, we have proposed a new algorithm for image reconstruction in optical interferometry. Previous RSC-based algorithmic frameworks have used the measured baseline phase as the primary observable (Lannes & Anterrieu 1999) and/or rely on computation of the Smith Normal Form (Lannes 2003). Our framework instead operates on those atmosphere-invariants available in a typical long-baseline interferometric imaging scenario, and leverages standard least-squares techniques tailored to the statistics of these observables. We have confirmed that the performance of the phase-estimation part of our algorithm can be easily quantified from first principles using standard linear estimation theory. Finally, we have conducted simulations at different photon-flux levels to corroborate this analysis, and to show the potential advantage of performing inference on the n-spectrum observable relative to its classical counterpart – the bi-spectrum. Large-scale optical systems such as the Planet Formation Imager are currently being designed to support ambitious missions including exoplanet observation. It is our hope that both the theoretical framework employed in this paper, as well as the

⁹ For our simulation, we used a MATLAB® implementation of Prim's algorithm which is available online (Greenbaum 2007)

Figure 14. (top row) Reconstructed images and convergence times for NLS algorithm with traditional-closure basis (left), generalized-closures from minimum cycle basis (middle), and generalized-closures from minimum-variance spanning tree (bottom row) Reconstructed images and elapsed running times with all $\binom{N^{ap}}{3}$ traditional closures at iteration 20 (left), iteration 40 (middle), and iteration 80 (right)

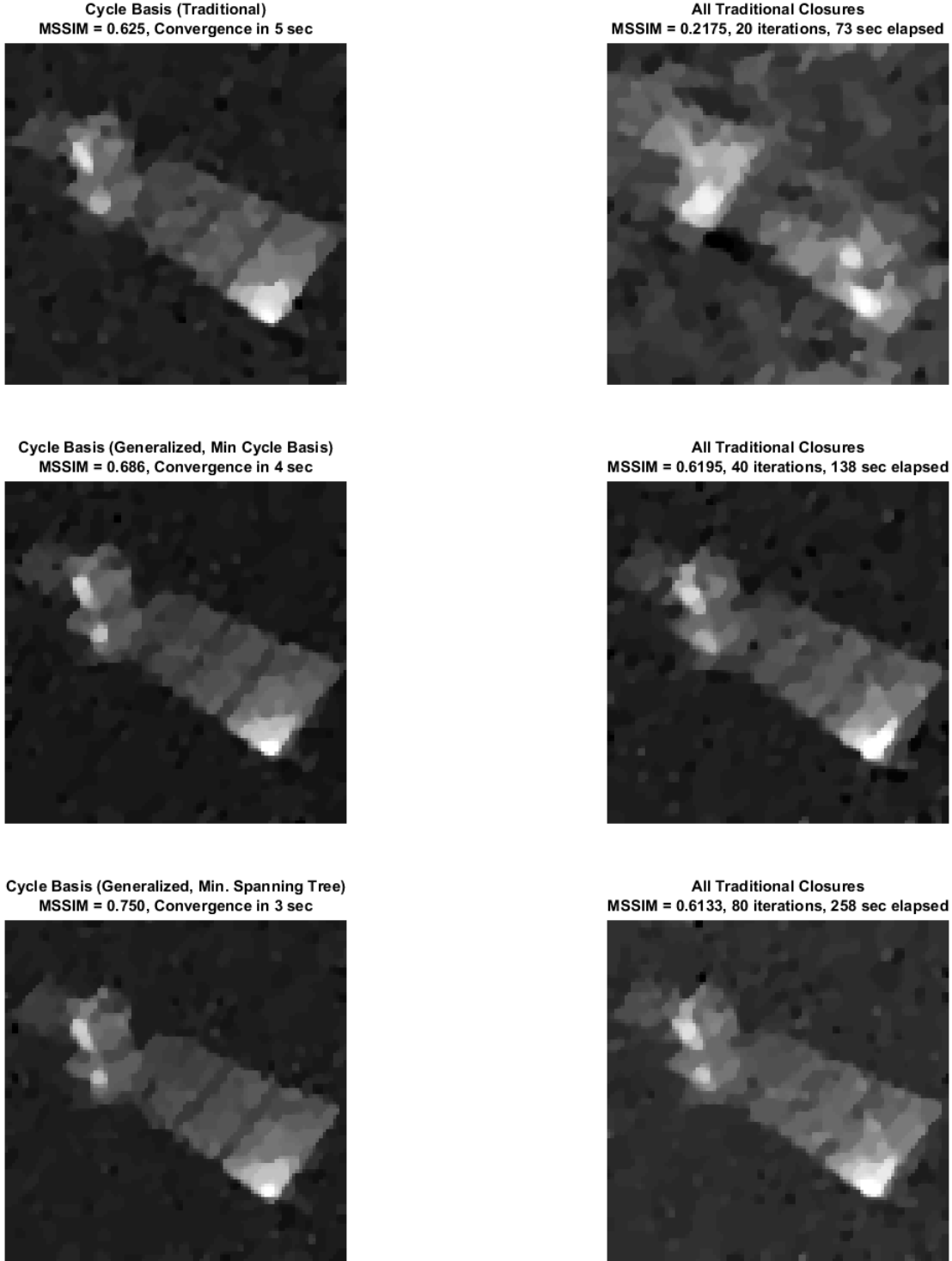
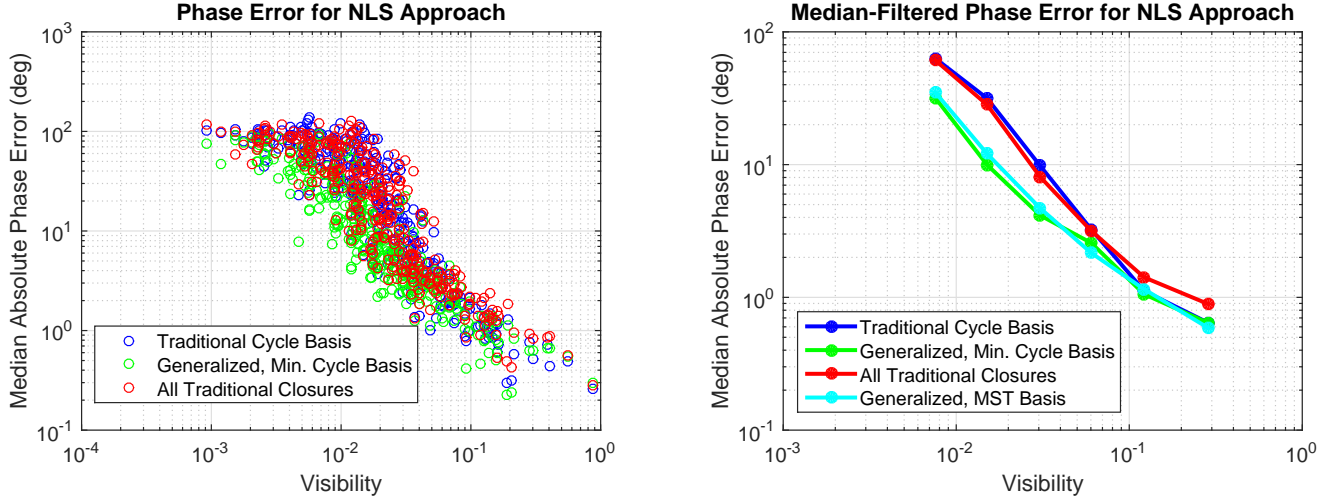
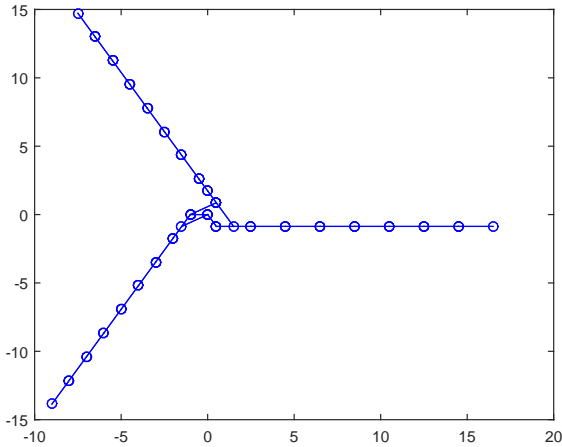


Figure 15. Raw (left) and median-filtered (right) Fourier phase error using the NLS approach.**Figure 16.** The minimum-variance spanning tree

practical algorithm itself, will prove useful to future users in designing **such** systems and processing their data.

ACKNOWLEDGEMENTS

ACKNOWLEDGEMENT: This work is sponsored by the Assistant Secretary of Defense for Research and Engineering under Air Force Contract FA8721-05-C-0002. Opinions, interpretations, conclusions, and recommendations are those of the author and are not necessarily endorsed by the United States Government.

Binoy Kurien would like to acknowledge the MATLAB-based software package NUFFT (Fessler 2003) developed by Prof. Jeff Fessler and his students at the University of Michigan. This software was used to create the image reconstruction results shown in this paper.

REFERENCES

Agrell E., Eriksson T., Vardy A., Zeger K., 2002, *IEEE Transactions on Information Theory*, 48, 2201
 Ali Z. S., et al., 2015, *The Astrophysical Journal*, 809, 61
 Arnot N., Atherton P., Greenaway A., Noordam J., 1985, *Traitem-
ment du Signal*, 2, 129
 Babai L., 1986, *Combinatorica*, 6, 1
 Baron F., Monnier J. D., Kloppenborg B., 2010, in *SPIE Astro-
nomical Telescopes+ Instrumentation*, pp 77342I-77342I
 Becker S., Bobin J., Candes E., 2011, *SIAM J. Imaging Sci.*, 4, 1
 Besnerais G. L., Lacour S., Mugnier L. M., Thiébaut E., Perrin G.,
 Meimon S., 2008, *IEEE Journal of Selected Topics in Signal
Processing*, 2, 767
 Bretscher O., 2001, *Linear Algebra with Applications*, 2nd edn.
 Prentice Hall, Upper Saddle River, New Jersey, USA
 Buscher D., 2015, *Practical Optical Interferometry*, 1st edn. Cam-
bridge University Press, Cambridge CB2 8BS, U.K.
 Candès E. J., Romberg J. K., Tao T., 2006, *Communications on
Pure and Applied Mathematics*, 59, 1207
 Casella G., Berger R., 2002, *Statistical Inference*, 2nd edn. Thom-
son Learning, Pacific Grove, CA
 Dijkstra E. W., 1959, *NUMERISCHE MATHEMATIK*, 1, 269
 Donoho D., 2006, *Information Theory*, *IEEE Transactions on*, 52,
 1289
 Fessler J., 2003, *NUFFT MATLAB Toolbox*,
 `http://web.eecs.umich.edu/~fessler/code/`
 Golay M. J. E., 1970, *J. Opt. Soc. Am.*, 61, 272
 Gordon, J. A. Buscher, D. F. 2012, *Astronomy and Astrophysics*,
 541, A46
 Gorham P., Ghez A., Kulkarni S., Nakajima T., Neugebauer G.,
 Oke J., Prince T., 1989, *Astronomical Journal*, 98, 1783
 Greenaway A. H., 1990, *Proc. SPIE 1351, Digital Image Synthesis
and Inverse Optics*, 1351, 738
 Greenaway A., 1994, in *NATO ASI Series. Series C: Mathematical
and Physical Sciences*, Vol. 423, *Adaptive Optics for Astron-
omy*. Kluwer Academic Publishers, Boston, USA
 Greenbaum A., 2007, *Prim's Algorithm*, Online:
 `https://www.math.washington.edu/~greenbau/Math
381/programs/prim.m`
 Gross J., Yellen J., 2006, *Graph Theory and its Applications*, 2nd
edn. Chapman and Hall, Boca Raton, FL, USA
 Hamaker J. P., O'Sullivan J. D., Noordam J. E., 1977, *J. Opt.
Soc. Am.*, 67, 1122
 Hill E., 2008, *CALIPSO Satellite*, Online:

http://calipsooutreach.hamptonu.edu/images/img_gallery/Satellite/index.html

Högberg J., 1974, *Astronomy and Astrophysics Supplement*, 15, 417

Horton J., 1987, *SIAM Journal on Computing*, 16, 358

Huby, E. et al., 2013, *A&A*, 560, A113

Ireland M. J., 2013, *Monthly Notices of the Royal Astronomical Society*, 433, 1718

Jennison R., 1958, *Monthly Notices of the Royal Astronomical Society*, 118, 276

Jovanovic N., et al., 2012, *Monthly Notices of the Royal Astronomical Society*, 427, 806

Kay S., 1993, *Fundamentals of Statistical Signal Processing, Vol. I Estimation Theory*, 1st edn. Prentice Hall, Upper Saddle River, NY

Kraus S., et al., 2014, in Rajagopal J. K., Creech-Eakman M. J., Malbet F., eds, *Optical and Infrared Interferometry IV Vol. 9146, Very High Angular Resolution Imaging*. Montreal, Quebec, Canada, pp 914611–914611–13

Kulkarni S., Prasad S., Nakajima T., 1991, *J. Opt. Soc. Am. A*, 8, 499

Kurien B. G., Rachlin Y., Shah V. N., Ashcom J. B., Tarokh V., 2014, in *Imaging and Applied Optics 2014*. Optical Society of America, p. SM2F.3, doi:10.1364/SRS.2014.SM2F.3

Kurien B. G., Tarokh V., Rachlin Y., Shah V. N., Ashcom J. B., 2016, *Monthly Notices of the Royal Astronomical Society*

Lacour S., Thiébaut E., Perrin G., 2007, *Monthly Notices of the Royal Astronomical Society*, 374, 832

Lannes A., 1991, *Inverse Problems*, 7, 261

Lannes A., 2003, in, Vol. 126, *Advances in Imaging and Electron Physics*. Academic Press, Boston, USA

Lannes A., Anterrieu E., 1999, *Journal of the Optical Society of America A*, 16, 2866

Liebchen C., Rizzi R., 2005, *Inf. Process. Lett.*, 94, 107

MATLAB 2014, version 8.4.0.150421 (R2014b). The MathWorks Inc., Natick, Massachusetts

Marthi V. R., Chengalur J., 2014, *Monthly Notices of the Royal Astronomical Society*, 437, 524

Martinache F., 2010, *The Astrophysical Journal*, 724, 464

Martinache F., 2014, in *Proceedings of Haute Provence Observatory Colloquium (23–27 September 2013)*. pp ??–??

Montgomery D., Peck E., Vining G., 2006, *Introduction to Linear Regression Analysis*, 4th edn. John Wiley and Sons, Inc., Hoboken, NJ, USA

Negrete-Regagnon P., 1996, *Opt. Lett.*, 21, 275

O'Connor D., 2012, The Bellman-Ford-Moore Shortest Path Algorithm, Online: <http://www.mathworks.com/matlabcentral/fileexchange/38129-the-bellman-ford-moore-shortest-path-algorithm>

Pearson T. J., Readhead A. C. S., 1984, *Annual Review of Astronomy and Astrophysics*, 22, 97

Perrin G., Lacour S., Woillez J., Thiébaut E., 2006, *Monthly Notices of the Royal Astronomical Society*, 373, 747

Prim R. C., 1957, *The Bell System Technical Journal*, 36, 1389

Readhead A., Nakajima T., Pearson T., Neugebauer G., Oke J., Sargent W., 1988, *Astronomical Journal*, 95, 1278

Ruderman D., 1994, *Network: Computation in Neural Systems*, 5, 517

Rudin L. I., Osher S., Fatemi E., 1992, *Phys. D*, 60, 259

Skilling J., Bryan R. K., 1984, *Monthly Notices of the Royal Astronomical Society*, 211, 111

Smith H., 1861, *Phil. Trans. R. Soc. Lond.*, 151, 293

Thiébaut E., 2013, *New Concepts in Imaging: Optical and Statistical Models*, 59, 157

Wang Z., Bovik A. C., Sheikh H. R., Simoncelli E. P., 2004, *IEEE Transactions on Image Processing*, 13, 600

Wiaux Y., Jacques L., Puy G., Scaife A. M. M., Vandergheynst P., 2009, *Monthly Notices of the Royal Astronomical Society*, 395, 1733

Wieringa M., 1992, *Experimental Astronomy*, 2, 203

Zernike F., 1938, *Physica*, 5, 785

Zheng H., Tegmark M., Buza V., Dillon J., 2014, *Monthly Notices of the Royal Astronomical Society*, 445, 1084

Zhou A., 2014, CLLL lattice reduction algorithm, Online: <http://www.mathworks.com/matlabcentral/fileexchange/45149-clll-lattice-reduction-algorithm>

Zmuidzinas J., 2003, *J. Opt. Soc. Am. A*, 20, 218

van Cittert P. H., 1934, *Physica*, 1, 201

APPENDIX A: FIZEAU VARIANCE APPROXIMATIONS

A1 Variance Decomposition

In this section we justify our approximation for the variance of the n-spectrum for the Fizeau architecture. Our goal here is not to compute all of the numerous terms in the variance, but rather to present the mathematical intuition behind the approximation we have used. The general formula for the variance of an n-spectra G is:

$$Var[G] = \left\langle \prod_{i=1}^t z_i z_i^* \right\rangle - \left\langle \prod_{i=1}^t z_i \right\rangle \left\langle \prod_{i=1}^t z_i^* \right\rangle \quad (A1)$$

For simplicity, we analyze the standard bispectrum case ($n = 3$). The analysis extends naturally to the n-spectrum. Note that by extension of Equation (5) the first term can be written as:

$$\left\langle \prod_{i=1}^t z_i z_i^* \right\rangle = \sum_{p_a, p_b, p_c, p_d, p_e, p_f} \langle q(p_a) q(p_b) q(p_c) q(p_d) q(p_e) q(p_f) \rangle \times e^{i\omega_1(p_d - p_a)} e^{i\omega_2(p_e - p_b)} e^{i\omega_3(p_f - p_c)} \quad (A2)$$

Similarly, the second term in Equation (A1) can be written as:

$$\begin{aligned} \left\langle \prod_{i=1}^t z_i \right\rangle \left\langle \prod_{i=1}^t z_i^* \right\rangle &= \sum_{p_a, p_b, p_c, p_d, p_e, p_f} \langle q(p_a) q(p_b) q(p_c) \rangle \langle q(p_d) q(p_e) q(p_f) \rangle \\ &\times e^{i\omega_1(p_d - p_a)} e^{i\omega_2(p_e - p_b)} e^{i\omega_3(p_f - p_c)} \quad (A3) \end{aligned}$$

Proceeding analogously to Equation (7), we utilize the general formula for the moments of a Poisson distribution to perform the following decomposition of the first factor in the summand in Equation (A2) (Kulkarni et al. 1991):

$$\langle q(p_a)q(p_b)q(p_c)q(p_d)q(p_e)q(p_f) \rangle = \quad (A4)$$

$$+ \langle q(p_a) \rangle \langle q(p_b) \rangle \langle q(p_c) \rangle \langle q(p_d) \rangle \langle q(p_e) \rangle \langle q(p_f) \rangle \quad (A5)$$

$$+ \delta_{p=p_a=p_d} \langle q(p) \rangle \langle q(p_b) \rangle \langle q(p_c) \rangle \langle q(p_e) \rangle \langle q(p_f) \rangle \quad (A6)$$

$$+ \delta_{p=p_b=p_e} \langle q(p) \rangle \langle q(p_a) \rangle \langle q(p_c) \rangle \langle q(p_d) \rangle \langle q(p_f) \rangle \quad (A7)$$

$$+ \delta_{p=p_c=p_f} \langle q(p) \rangle \langle q(p_a) \rangle \langle q(p_b) \rangle \langle q(p_d) \rangle \langle q(p_e) \rangle \quad (A8)$$

$$+ \delta_{p=p_a=p_d} \langle q(p) \rangle \delta_{p'=p_b=p_e} \langle q(p') \rangle \langle q(p_c) \rangle \langle q(p_f) \rangle \quad (A9)$$

$$+ \delta_{p=p_a=p_d} \langle q(p) \rangle \delta_{p'=p_c=p_f} \langle q(p') \rangle \langle q(p_b) \rangle \langle q(p_e) \rangle \quad (A10)$$

$$+ \delta_{p=p_b=p_e} \langle q(p) \rangle \delta_{p'=p_c=p_f} \langle q(p') \rangle \langle q(p_a) \rangle \langle q(p_c) \rangle \quad (A11)$$

$$+ \delta_{p=p_a=p_d} \langle q(p) \rangle \delta_{p'=p_b=p_e} \langle q(p') \rangle \delta_{p''=p_c=p_f} \langle q(p'') \rangle \quad (A12)$$

$$+ \delta_{p=p_a=p_e} \langle q(p) \rangle \langle q(p_b) \rangle \langle q(p_c) \rangle \langle q(p_d) \rangle \langle q(p_f) \rangle \quad (A13)$$

$$+ \delta_{p=p_a=p_f} \langle q(p) \rangle \langle q(p_b) \rangle \langle q(p_c) \rangle \langle q(p_d) \rangle \langle q(p_e) \rangle \quad (A14)$$

$$+ \delta_{p=p_b=p_d} \langle q(p) \rangle \langle q(p_a) \rangle \langle q(p_c) \rangle \langle q(p_e) \rangle \langle q(p_f) \rangle \quad (A15)$$

$$+ \delta_{p=p_b=p_f} \langle q(p) \rangle \langle q(p_a) \rangle \langle q(p_c) \rangle \langle q(p_d) \rangle \langle q(p_e) \rangle \quad (A16)$$

$$+ \delta_{p=p_c=p_d} \langle q(p) \rangle \langle q(p_a) \rangle \langle q(p_b) \rangle \langle q(p_e) \rangle \langle q(p_f) \rangle \quad (A17)$$

$$+ \delta_{p=p_c=p_e} \langle q(p) \rangle \langle q(p_a) \rangle \langle q(p_b) \rangle \langle q(p_d) \rangle \langle q(p_f) \rangle \quad (A18)$$

$$+ \delta_{p=p_a=p_b} \langle q(p) \rangle \langle q(p_c) \rangle \langle q(p_d) \rangle \langle q(p_e) \rangle \langle q(p_f) \rangle \quad (A19)$$

$$+ \delta_{p=p_a=p_c} \langle q(p) \rangle \langle q(p_b) \rangle \langle q(p_d) \rangle \langle q(p_e) \rangle \langle q(p_f) \rangle \quad (A20)$$

$$+ \delta_{p=p_b=p_c} \langle q(p) \rangle \langle q(p_a) \rangle \langle q(p_d) \rangle \langle q(p_e) \rangle \langle q(p_f) \rangle \quad (A21)$$

$$+ \delta_{p=p_d=p_e} \langle q(p) \rangle \langle q(p_a) \rangle \langle q(p_b) \rangle \langle q(p_c) \rangle \langle q(p_f) \rangle \quad (A22)$$

$$+ \delta_{p=p_a=p_d} \langle q(p) \rangle \langle q(p_a) \rangle \langle q(p_b) \rangle \langle q(p_c) \rangle \langle q(p_e) \rangle \quad (A23)$$

$$+ \delta_{p=p_e=p_f} \langle q(p) \rangle \langle q(p_a) \rangle \langle q(p_b) \rangle \langle q(p_c) \rangle \langle q(p_d) \rangle \quad (A24)$$

$$+ \delta_{p=p_a=p_b=p_c} \langle q(p) \rangle \langle q(p_d) \rangle \langle q(p_e) \rangle \langle q(p_f) \rangle \quad (A25)$$

$$\dots + \text{other third-order terms} \quad (A26)$$

$$+ \delta_{p=p_a=p_b=p_c=p_d} \langle q(p) \rangle \langle q(p_e) \rangle \langle q(p_f) \rangle \quad (A27)$$

$$\dots + \text{other fourth-order terms} \quad (A28)$$

$$\dots \text{etc.} \quad (A29)$$

The total number of partitions (203) in the summation above is given by the 6th Bell number. Below we categorize the terms by their order, which in this case we define as the largest number of common pixels in each partition. We will see that we can approximate the pseudo-variance to reasonable accuracy by including a particular subset of the Order-2 terms. Note that all terms in the analogous decomposition of Equation (A3) are also in Equation (A2) and hence cancel them in Equation (A1).

A2 Order-2 Terms

These terms have a pair of common pixels. We distinguish between the following two cases:

Case 1: conjugate pairs These terms are given in (A6)-(A12). The common pixels belong to the conjugate pairs, i.e. $p := p_a = p_d$, $p := p_b = p_e$, and $p := p_c = p_f$, respectively, which also appear in the pairwise case. Let us assume that the visibilities associated with ω_1 , ω_2 , and ω_3 are all roughly equal, i.e. $\bar{\gamma} = \gamma_1 = \gamma_2 = \gamma_3$. Consider the sum of the first of these terms (A6) over the focal plane, i.e.:

$$\begin{aligned} & \sum_{p=p_a=p_d, p_b, p_c, p_e, p_f} \langle q(p) \rangle \langle q(p_b) \rangle e^{i\omega_2 p_b} \langle q(p_c) \rangle e^{i(\omega_1+\omega_2)p_c} \\ & \times \langle q(p_e) \rangle e^{-i\omega_2 p_e} \langle q(p_f) \rangle e^{-i(\omega_1+\omega_2)p_f} \\ & = \sum_{p:=p_a=p_d} \Lambda_p \sum_{p_b} \Lambda_{p_b} e^{i\omega_2 p_b} \sum_{p_c} \Lambda_{p_c} e^{i(\omega_1+\omega_2)p_c} \\ & \sum_{p_e} \Lambda_{p_e} e^{i\omega_2 p_e} \sum_{p_f} \Lambda_{p_f} e^{-i(\omega_1+\omega_2)p_f} \end{aligned} \quad (A30)$$

The magnitude of this expression is $(N_{ap}n^5\gamma_2^2\gamma_3^3)$. In the case where all visibilities are equal to $\bar{\gamma}$, this expression becomes $N_{ap}n^5\bar{\gamma}^4$. Terms (A7)-(A8) follow this same form.

Now consider term (A9):

$$\begin{aligned} & \sum_{p=p_a=p_d, p'=p_b=p_e, p_f} \langle q(p) \rangle \langle q(p') \rangle \langle q(p_e) \rangle e^{-i\omega_2 p_e} \\ & \times \langle q(p_f) \rangle e^{-i(\omega_1+\omega_2)p_f} \\ & = \sum_{p:=p_a=p_d} \Lambda_p \sum_{p':=p_b=p_e} \Lambda'_p \sum_{p_c} \Lambda_{p_c} e^{i(\omega_1+\omega_2)p_f} \\ & \times \sum_{p_f} \Lambda_{p_f} e^{-i(\omega_1+\omega_2)p_f} \end{aligned} \quad (A31)$$

The magnitude of this expression is $N_{ap}^2 n^4 \gamma_3^2$, which, under the assumption of equal visibilities, becomes $N_{ap}^2 n^4 \bar{\gamma}^2$. Terms (A10)-(A11) follow this same form.

Case 2: mixed non-conjugate pairs

We now consider the terms in which a pair includes two distinct baselines (e.g. (A13)-(A18)). The common pixels in this case are such that one of the corresponding baselines is conjugated and the other is not. Taking, for example, the case (A13) in which $p := p_a = p_e$, we have:

$$\begin{aligned} & \sum_{p=p_a=p_e, p_b, p_c, p_d, p_f} \langle q(p) \rangle e^{i(\omega_1-\omega_2)p} \langle q(p_b) \rangle e^{i\omega_2 p_b} \\ & \times \langle q(p_c) \rangle e^{i(\omega_1+\omega_2)p_c} \langle q(p_d) \rangle e^{-i\omega_2 p_d} \langle q(p_f) \rangle e^{-i(\omega_1+\omega_2)p_f} \\ & = \sum_{p:=p_a=p_e} \Lambda_p e^{i(\omega_1-\omega_2)p} \sum_{p_b} \Lambda_{p_b} e^{i\omega_2 p_b} \sum_{p_c} \Lambda_{p_c} e^{i(\omega_1+\omega_2)p_c} \\ & \times \sum_{p_d} \Lambda_{p_d} e^{-i\omega_2 p_d} \sum_{p_f} \Lambda_{p_f} e^{-i(\omega_1+\omega_2)p_f} \end{aligned} \quad (A32)$$

where $\gamma_{\omega_1-\omega_2}$ is the visibility of the fringe of spatial frequency $\omega_1 - \omega_2$. Note that the first factor in the Equation above clearly vanishes if such a fringe is not created by the beam combiner. Otherwise, assuming equal strength of the visibilities, the magnitude of this expression is given by $(n^5 \gamma_{\omega_1-\omega_2} \gamma_1 \gamma_2 \gamma_3^2)$, or $n^5 \bar{\gamma}^5$ in the case of equal visibilities. Comparing with any of the Case 1 terms and recalling that $\bar{\gamma} < 1$, we see that the latter will dominate the former in the regime considered in this paper ($n \approx 1e3$, $\bar{\gamma} \ll 1$, $N_{ap} = 31$).

Case 3: terms in decomposition Equation (A3)

This Case includes terms (A5), as well as (A19)-(A24). The common pixels are such that both or neither of the corresponding baselines are conjugated, i.e.: the cases $p_a = p_b$, $p_a = p_c$, $p_b = p_c$, $p_d = p_e$, $p_d = p_f$, $p_e = p_f$. These terms are canceled by their counterparts in Equation (A2). \square

A3 Higher Order Terms

An example of a third-order term would be the case of $p := p_a = p_b = p_d$, whose sum is given by:

$$\sum_{p:=p_a=p_b=p_d, p_c, p_e, p_f} \langle q(p) \rangle e^{i\omega_2 p} \langle q(p_c) \rangle e^{-i(\omega_1+\omega_2)p_c} \langle q(p_e) \rangle e^{-i\omega_2 p_e} \langle q(p_f) \rangle e^{-i(\omega_1+\omega_2)p_f} \quad (A33)$$

$$= \sum_{p:=p_a=p_b=p_d} \Lambda_p e^{i\omega_2 p} \sum_{p_c} \Lambda_{p_c} e^{i(\omega_1+\omega_2)p_c} \sum_{p_e} \Lambda_{p_e} e^{-i\omega_2 p_e} \sum_{p_f} \Lambda_{p_f} e^{-i(\omega_1+\omega_2)p_f} \quad (A34)$$

The magnitude of this expression is given by $n^4 \gamma_2^2 \gamma_3^2$. For equal visibilities, we have $n^4 \bar{\gamma}^4$. Clearly this term will be dominated by the Case 1 terms. Other high-order terms exhibit a similar sharp attenuation which allows them to be neglected for practical purposes. \square

Given the relative strengths of the terms shown above, we will retain Case 1 terms (A6)-(A12), which after summation and factoring, yield Equation (38). Note that this amounts to the following approximation:

$$V_{fizeau}(G) \approx \left[\prod_{i=1}^t \langle z_i z_i^* \rangle \right] - \prod_{i=1}^t \langle z_i \rangle \langle z_i^* \rangle \quad (A35)$$

Applying these same approximations leads to the Fizeau covariance expressions in Equations (40)-(41).

APPENDIX B: PROOF OF INJECTIVITY OF THE RSC CLOSURE MAPPING

Proposition B.1: For a valid RSC array, the columns $\Delta\mathbf{r}_x$ and $\Delta\mathbf{r}_y$ form a basis for the two-dimensional nullspace of \mathbf{C}_{oc} .

Proof: To see that the two columns mentioned belong to the nullspace of \mathbf{C}_{oc} , note that each solution set to the noiseless version of Equation (46) above remains valid after replacing each θ_{ij} with $\theta_{ij}^p = \theta_{ij} - \mathbf{z} \cdot (\mathbf{r}_i - \mathbf{r}_j)$.

We then need to establish that these two vectors span the entire nullspace of \mathbf{C}_{oc} by showing that this nullspace is two-dimensional. Suppose we have a vector \mathbf{w} which is in the nullspace \mathbf{C}_{oc} . This is equivalent to the either of the following conditions: $\mathbf{M}_\theta \mathbf{w} = \mathbf{0}$, or $\mathbf{M}_\theta \mathbf{w} \in \text{ker}(\mathbf{C}_{mc})$. The former condition is not possible since the columns spanning the subspace K are linearly-independent. The latter condition is equivalent to the condition that $\mathbf{M}_\theta \mathbf{w} \in K \cap L$. It is well-known fact that for any two subspaces K and L , we have:

$$\dim(K \cap L) = \dim(K) + \dim(L) - \dim(K + L) \quad (B1)$$

We established in Section 3.1 that $\dim(K + L) = \text{rank}(\mathbf{M}) = d + N - 3$ for a valid RSC system. Also $\dim(K) = d$, since the K is spanned by d linearly-independent columns. Finally $\dim(L) = N - 1$. Substituting into Equation (B1), we see that $\dim(K \cap L) = 2$. \square

Corollary B.2: For a valid RSC array, the mapping \mathbf{C}_{oc} is injective up to an image shift.

Proof: Proposition B.1 showed that the nullspace is comprised of linear combinations of vectors $\Delta\mathbf{r}_x$ and $\Delta\mathbf{r}_y$. Note that $\Delta\mathbf{r}_x$ and $\Delta\mathbf{r}_y$ are simply scaled versions of the x - and y -spatial frequency vectors in the array, respectively. Hence adding linear combinations of these vectors to a particular RSC phase solution merely produces phase ramps in the Fourier domain, which are equivalent to translations (or shifts) in the image domain. In other words, the mapping \mathbf{C}_{oc} is invertible up to an unknown image shift. \square

APPENDIX C: PROOF OF PROPOSITION 3.2

We begin the Proof with the following Lemma:

Lemma C.1: The final 2 columns of \mathbf{V}_σ form a basis for the nullspace of \mathbf{C}_{oc} .

Proof: This follows from the fact \mathbf{C}_{oc} is rank-deficient by 2, and standard properties of the right singular vectors comprising \mathbf{V}_σ in the SVD. (Bretscher 2001) \square

Note that the error resulting from application of the pseudo-inverse \mathbf{C}_{oc}^+ to the unwrapped vector of closures will be given by:

$$2\pi \mathbf{e}_\sigma = \mathbf{C}_{oc}^+ (2\pi \mathbf{e}_h^*) \quad (C1)$$

Let us express the spatial frequencies measured by an array as two-element vectors of the form (ω_x, ω_y) . Let \mathbf{X} be the $d \times 2$ matrix containing these spatial frequencies. Note then that the phase-wrap error will manifest itself merely as an image shift if and only if this error is a (modulo- 2π) phase ramp, i.e. there exists a 2-element shift vector \mathbf{z} and an integer vector \mathbf{k} which together satisfy:

$$2\pi \mathbf{e}_\sigma - 2\pi \mathbf{X} \mathbf{z} = 2\pi \mathbf{k} \quad (C2)$$

Substituting from Equation (C1) we obtain:

$$\mathbf{C}_{oc}^+ (2\pi \mathbf{e}_h^*) - 2\pi \mathbf{X} \mathbf{z} = 2\pi \mathbf{k} \quad (C3)$$

Dividing through by 2π we obtain the equation: $\mathbf{C}_{oc}^+ \mathbf{e}_h^* - \mathbf{X} \mathbf{z} = \mathbf{k}$. Note that each element of \mathbf{C}_{oc}^+ can be expressed as some rational number $\frac{p_i}{q_i}$. Similarly we first assume \mathbf{X} contains rational spatial frequencies with greatest common denominator q_x . Then we can multiply through by the least-common-multiple (LCM) of the $\{q_i\}$ and q_x to obtain a system of equations whose coefficients are guaranteed to be integer (i.e., we have a linear Diophantine system). Let this LCM be denoted as l . Then we have, after rearranging terms,

$$l \mathbf{X} \mathbf{z} = l(\mathbf{C}_{oc}^+ \mathbf{e}_h^* - \mathbf{k}) \quad (C4)$$

We now wish to determine conditions under which there exist vectors \mathbf{k} and \mathbf{z} satisfying this overdetermined Diophantine system. Applying the Smith Normal Form decomposition (c.f. Theorem 3.1) to the matrix $l \mathbf{X}$ this time, and noting that $\text{rank}(\mathbf{X}) = 2$, we have:

$$\mathbf{D}_\mathbf{X} = \mathbf{U}_\mathbf{X} (l \mathbf{X}) \mathbf{V}_\mathbf{X} \quad (C5)$$

where $\mathbf{U}_\mathbf{X}$ and $\mathbf{V}_\mathbf{X}$ are unimodular matrices of size $m \times m$ and

2×2 , respectively, and \mathbf{D}_X is a rectangular diagonal matrix whose entries are zero below row 2.

If we left-multiply Equation (C4) by \mathbf{U}_X on both sides, we obtain:

$$l\mathbf{U}_X\mathbf{X}z = l\mathbf{U}_X(\mathbf{C}_{oc}^+ e_h^* - k) \quad (\text{C6})$$

Using Equation (C5) and the fact that \mathbf{V}_X is a unimodular (and hence invertible) matrix, we can then write:

$$\mathbf{D}_X\mathbf{V}_X^{-1}z = l(\mathbf{U}_X\mathbf{C}_{oc}^+ e_h^* - \mathbf{U}_Xk) \quad (\text{C7})$$

We are now in position to prove the main result of this section, which is preceded by the following Lemma:

Lemma C.2: Given wrap-invariance, the (column) vector $\mathbf{U}_X\mathbf{C}_{oc}^+ e$ has integer entries below row 2.

Proof:

Given that the elementary divisors of \mathbf{C}_{oc} are all 1, we know there exists an integer vector k_0 such that:

$$e_h^* = \mathbf{C}_{oc}k_0 \quad (\text{C8})$$

Substituting Equations (C8) and (60) into Equation (C1), we obtain:

$$e_\sigma = \mathbf{V}_\sigma\mathbf{\Sigma}_\sigma^+\mathbf{U}_\sigma^T\mathbf{U}_\sigma\mathbf{\Sigma}_\sigma\mathbf{V}_\sigma^Tk_0 \quad (\text{C9})$$

Noting that \mathbf{U}_σ is orthogonal, this equation can be simplified to

$$e_\sigma = (\mathbf{V}_\sigma - \mathbf{N})\mathbf{V}_\sigma^Tk_0 \quad (\text{C10})$$

where \mathbf{N} is a matrix of the same size as \mathbf{V}_σ , which is zero except for the last two columns. These last two columns are identical to those of \mathbf{V}_σ , and hence by Lemma 4.1 comprise an orthogonal basis for the nullspace of \mathbf{C}_{oc} . Noting the orthogonality of \mathbf{V}_σ , this can be further simplified to:

$$e_\sigma = k_0 - \mathbf{N}\mathbf{V}_\sigma^Tk_0 \quad (\text{C11})$$

Note that each of the two non-zero column vectors $\{v_k\}, k \in 1, 2$ in \mathbf{N} can be expressed as a linear combinations of the elements of the canonical basis for the nullspace of \mathbf{C}_{oc} given in Section 3, i.e.

$$v_k = a_1 w_1 + a_2 w_2 \quad (\text{C12})$$

Hence we have:

$$\mathbf{U}_Xe_\sigma = \mathbf{U}_Xk_0 - \mathbf{U}_X\mathbf{N}_K\mathbf{V}_\sigma^Tk_0 \quad (\text{C13})$$

Since \mathbf{U}_X is an integer matrix, the first term is clearly integral. Let us then examine the second term, and in particular, the product $\mathbf{U}_X\mathbf{N}$. By substitution from Equation (C12), we see that or any of the two non-zero columns v_k of \mathbf{N} , we have:

$$\mathbf{U}_Xv_K = a_1\mathbf{U}_Xw_1 + a_2\mathbf{U}_Xw_2 \quad (\text{C14})$$

Now note from Theorem 3.1 that \mathbf{U}_X is a matrix which annihilates all the spatial frequencies in the matrix \mathbf{X} below

row 2. But recall from Section 3 that these spatial frequencies are the contents of the two columns w_1 and w_2 (up to a uniform scaling factor). Therefore the column vector in Equation (C14) is zero below row 2. This means in turn that the second term in Equation (C13) is zero below row 2, and hence that \mathbf{U}_Xe_σ is integral below row 2 (since the first term is integral). \square

To utilize Lemma C.2, we first re-arrange the Equation (C7) above so that it reads:

$$\frac{1}{l}\mathbf{D}_X\mathbf{V}_X^{-1}z - \mathbf{U}_X\mathbf{C}_{oc}^+ e_h^* = -\mathbf{U}_Xk \quad (\text{C15})$$

Let $v = \frac{1}{l}\mathbf{D}_X\mathbf{V}_X^{-1}z - \mathbf{U}_X\mathbf{C}_{oc}^+ e_h^*$. Note that since \mathbf{D}_X is zero below row 2, the entries of v below row 2 will be equal to those of $(-\mathbf{U}_X\mathbf{C}_{oc}^+ e_h^*)$, which are integers by Lemma C.2. Now consider the first and second entries of v . Let f be the vector containing the fractional parts of the first two elements of vector $\mathbf{U}_X\mathbf{C}_{oc}^+ e_h^*$, and let \mathbf{A} be the invertible matrix consisting of the first two rows of $\frac{1}{l}\mathbf{D}_X\mathbf{V}_X^{-1}$. Without loss of generality, choose $z^* = \mathbf{A}^{-1}f$ so that the fractional part f is annihilated, leaving only integer elements in the first two entries of v . Hence we now have:

$$v = -\mathbf{U}_Xk \quad (\text{C16})$$

with v ensured to contain only integer elements. Since \mathbf{U}_X is unimodular, the vector $k^* = -\mathbf{U}_X^{-1}v$ will be integral. We have thus found a pair (z^*, k^*) with integer k^* which satisfies the Equation (C7). Since Equation (C7) is related to Equation (C4) via a unimodular (and hence invertible) mapping \mathbf{U}_X , invariance is hence proven. \square

This paper has been typeset from a TeX/LaTeX file prepared by the author.